Atmos. Meas. Tech. Discuss., 8, 8295–8352, 2015
www.atmos-meas-tech-discuss.net/8/8295/2015/
doi:10.5194/amtd-8-8295-2015

Atmospheric Measurement Techniques Discussions
Open Access

Global cloud top height retrieval using SCIAMACHY limb spectra: model studies and first results

K.-U. Eichmann[1], L. Lelli[1], C. von Savigny[2], H. Sembhi[3], and J. P. Burrows[1]

[1]Institute of Environmental Physics, University of Bremen, Bremen, Germany
[2]Institute of Physics, Ernst Moritz Arndt University of Greifswald, Greifswald, Germany
[3]Earth Observation Science, University of Leicester, Leicester, UK

Received: 5 May 2015 – Accepted: 16 July 2015 – Published: 10 August 2015

Correspondence to: K.-U. Eichmann (eichmann@uni-bremen.de)

Published by Copernicus Publications on behalf of the European Geosciences Union.

Abstract

Cloud top heights (CTH) were retrieved for the period 1 January 2003 to 7 April 2012 using height-resolved limb spectra measured with the Scanning Imaging Absorption spectroMeter for Atmospheric CHartographY (SCIAMACHY) on board ENVISAT (ENVIronmental SATellite). In this study, we tested the sensitivity of the colour index method used in the retrieval code SCODA (SCIAMACHY Cloud Detection Algorithm) and the accuracy of the retrieved CTHs in comparison to other methods. Sensitivity studies using the radiative transfer model SCIATRAN showed that the method is capable of generally detecting cloud tops down to about 5 km and very thin cirrus clouds even up to the tropopause. Volcanic particles can also be detected that occasionally reach the lower stratosphere. Low clouds at 2–3 km can only be retrieved under very clean atmospheric conditions, as light scattering of aerosols interferes with the cloud retrieval. Upper tropospheric ice clouds are detectable for cloud optical depths down to about τ_N=0.005, which is in the subvisual range. The detection sensitivity decreases towards the surface. An optical thickness of roughly 0.1 was the lower detection limit for water cloud top heights at 5 km. This value is much lower than thresholds reported for the passive cloud detection in nadir viewing direction.

Comparisons with SCIAMACHY nadir cloud top heights, calculated with the Semi-Analytical CloUd Retrieval Algorithm (SACURA), showed a good agreement in the global cloud field distribution. But only opaque clouds (τ_N >5) are detectable with the nadir passive retrieval technique in the UV-visible and infrared wavelength range. So due to the frequent occurrence of thin and sub-visual cirrus clouds in the tropics, large cloud top height deviations were detected between both viewing geometries. Also the land/sea contrast seen in nadir retrievals was not detected in limb mode. Co-located cloud top height measurements of the limb viewing Michelson Interferometer for Passive Atmospheric Sounding (MIPAS) on ENVISAT for the period from January 2008 to March 2012 were compared, showing good agreement to within 1 km, which is smaller than the vertical field of view of both instruments.

AMTD
8, 8295–8352, 2015

Lower stratospheric aerosols from volcanic eruptions occasionally interfered with the cloud retrieval and inhibited detection of tropospheric clouds. Examples of the impact of these events are shown for the volcanoes Kasatochi in August 2008, Sarychev Peak in June 2009, and Nabro in June 2010. Long-lasting aerosol layers were detected after these events in the Northern Hemisphere down to the tropics. Particle top heights up to about 22 km were retrieved in 2009, when the enhanced lower stratospheric aerosol layer persisted for about 7 months. Up to about 82 % of the Northern hemispheric lower stratosphere between 30° and 70° was covered by scattering particles in August 2009 and nearly half in October 2008.

1 Introduction

Clouds occur in complex shapes at a wide variety of scales in the Earth's atmosphere. The physical cloud parameters, e.g. optical thickness, albedo, and bottom/top heights from near the ground up to the tropopause are highly variable. Clouds cover about 2/3 of the Earth depending on the used optical thickness threshold (Stubenrauch et al., 2013). They are composed of liquid particles (T >0 °C), ice ($T \approx <$ −38 °C), or a mixed phase for intermediate temperatures (Boucher et al., 2013).

Clouds also have a large impact on the Earth's radiative balance and play a major, yet still relatively uncertain, role in the changing energy budget (IPCC, 2013). Depending on cloud type and height, they exert a cloud radiative effect which depends on the balance between cloud albedo and greenhouse forcing. The knowledge of global cloud characteristics is essential in different fields of numerical analyses, e.g. weather prediction, circulation, or climate change models.

A high percentage of the incoming visible light is scattered back to space due to the high albedo of optically thick clouds. The enhancement of the global, annual albedo is about −50 Wm^{-2}. Additionally infra–red (terrestrial) radiation is absorbed by clouds and then emitted again. This re-emission strongly depends on cloud temperature and

AMTD
8, 8295–8352, 2015

is annually and globally averaged in the order of 30 Wm^{-2}. The balance between these effects is also determined by the cloud properties (Boucher et al., 2013).

The light scattering ability of cloud droplets is only weakly wavelength dependent when compared to light scattered by molecules. Furthermore, light entering the cloud will encounter enhanced path lengths as it is scattered multiple times at the water or ice particles inside the cloud. This also enhances light absorption by trace gases in and above the clouds.

Tropical clouds can reach heights of roughly 17 km. These are either deep convective clouds or the more common cirrus clouds, which are mainly observed in the tropical tropopause layer (TTL) above 14 km (Fueglistaler et al., 2009). Cirrus clouds are mainly formed in the upper troposphere (above 8 km) by condensation nuclei such as mineral dust and metallic particles via heterogeneous freezing, while larger biological particles are removed by deposition before reaching these altitudes. They are either produced by the uplift of humid air or by a convective blow-off from deep convection. Due to the low temperatures at these heights (< −30 °C), cirrus clouds are made of small ice crystals (Cziczo et al., 2013).

In 84 % of the measurements of Cloud-Aerosol Lidar and Infrared Pathfinder Satellite Observations (CALIPSO) cirrus layers have a vertical extension of less than 1.5 km at heights between 13 and 16 km (Massie et al., 2007). Only 1.5 % of the cirrus have a thickness of more than 3 km. Lidar measurements made on the Space Shuttle have shown that thin cirrus layers near the tropopause can be down to 0.5 km thick and have a horizontal extent up to a few 1000 km (Winker et al., 1998).

Cirrus clouds are categorized as (a) subvisual, that is optically very thin with cloud optical depths (COD) τ_N <0.03, (b) thin ($0.03 < \tau_N < 0.3$), or (c) opaque ($\tau_N > 0.3$) (Sassen and Cho, 1992). Subvisual clouds are mainly found in the tropics with higher occurrence frequencies over oceans and during the night. Thin cirrus clouds are more frequent at night and are found mainly over equatorial land masses and the western Pacific. Moreover opaque cirrus clouds are mainly found during the day over oceans (Sassen et al., 2009). Cirrus cloud occurrence frequencies (or cloud fraction, CF) are

AMTD
8, 8295–8352, 2015

also coupled to dynamic circulation patterns. Davis et al. (2013) reported that TTL thin cirrus cloud fractions are partly driven by the quasi-biennial oscillation (QBO) and the upwelling in the tropical branch of the Brewer-Dobson circulation (BDC). For example, a reduced BDC upwelling and a warm QBO westerly phase increase the TTL temperature and reduce the relative humidity, which in turn leads to a reduction of the cloud fraction.

High-altitude, optically thin clouds are nearly transparent for the incoming shortwave solar radiation, but they partially absorb the outgoing Earth's longwave radiation. As the cloud particles are much colder than the surface, they re-emit comparatively little radiation towards space. The net effect is a warming of the atmosphere below the cloud ("cloud greenhouse forcing").

Low clouds (CTH $z_{ct} < 3$ km) on the other hand are the main contributor to an enhancement of the global albedo. They can also be optically thin ($\tau_N < 1$). Leahy et al. (2012) found that nearly half of all clouds over non-polar oceans have low tops of $z_{ct} < 3$ km. These clouds have an horizontal extent in the order of 2 km. Approximatively 45 % of all clouds are high-level (below 440 hPa, above 6.5 km), 15 % mid-level, and 40 % low-level (above 680 hPa, below 3.2 km) clouds (IPCC, 2013).

Different methods exist now to measure cloud properties from space. Nadir viewing, passive instruments (e.g. GOME, SCIAMACHY) were mainly designed to derive trace gas columns (Burrows et al., 1995; Bovensmann et al., 1999). But they can also retrieve cloud top heights using the strongest absorption band of molecular oxygen (i.e. O_2-A band: 755–775 nm) (Koelemeijer et al., 2002; Rozanov et al., 2004; Lelli et al., 2012). The height accuracy of these methods is within a few hundred meters. But retrievals are restricted to cloud optical depths larger than 5. Based on the International Satellite Cloud Climatology Project (ISCCP) D2 dataset, a global COD $\tau_N = 3.9 \pm 0.3$ was found by Rossow and Schiffer (1999) showing that a lot of clouds types cannot be retrieved. All forms of cirrus clouds ($\tau_N = 2.2$) with a 19.6 % global coverage are not detectable using passive nadir observations.

AMTD
8, 8295–8352, 2015

A number of satellite missions are specially designed for the detection of cloud properties. A comparison of these instruments with the ISCCP multi-spectral imager data has been performed by Stubenrauch et al. (2013). An average global cloud amount of about 68 % was reported for clouds with optical depths higher than 0.1. This increases to 73 % when also taking the subvisible cirrus clouds into account (Winker et al., 2009; Chepfer et al., 2010).

An easy way of passively measuring thin clouds is offered by sensors observing the atmosphere in limb geometry. For instance, the SAGE instrument detected very thin clouds ($\tau_N > 0.03$) and derived a high global cloud amount of 95 %. This is mainly due to the long light path of about 200 km around the tangent point increasing the number of cloud measurements (Stubenrauch et al., 2012). The Optical Spectrograph and Infrared Imaging System (OSIRIS) on-board Odin is a limb viewing instrument that can accurately measure thin cirrus cloud fractions and top heights using information from the 1530 nm IR channel (Bourassa et al., 2005) and the optical thickness of subvisual cirrus clouds at 750 nm (Normand et al., 2013). The High Resolution Dynamics Limb Sounder (HIRDLS) on-board the AURA spacecraft detects cirrus clouds, deep convective clouds and PSCs using infrared radiances at 12.1 µm (Massie et al., 2007). MIPAS on ENVISAT detected similar cloud parameters using bands in the regions MWIR (Mid Wavelength InfraRed) and TIR (Thermal InfraRed) (Spang et al., 2012; Sembhi et al., 2012). The Cloud-Aerosol Lidar with Orthogonal Polarization (CALIOP) aboard the CALIPSO satellite uses laser wavelengths of 532 and 1064 nm to measure e.g. physical cloud tops with high accuracy of about 60 m in the troposphere (Winker et al., 2009). Thin clouds with an optical thickness of about 0.01 are still detectable with this technique.

When retrieving atmospheric trace gas concentrations in the lower stratosphere/upper troposphere from limb measurements, clouds in the field of view influence the retrieval accuracy. It was thus necessary to omit the cloud contaminated part of the measurement profile in the retrieval algorithm to minimize trace gas errors at the heights above a cloud (Sonkaew et al., 2009). The SCODA retrieval scheme (SCIA-

AMTD
8, 8295–8352, 2015

MACHY ClOud Detection Algorithm) was developed using the colour ratio method because of these results. It was added to the SCIAMACHY level 2 operational processor (version 5.04) (ESA, 2013) to improve the limb trace gas retrievals towards the troposphere. It was also used for scientific profile retrievals of upper tropospheric/lower stratospheric water vapour and trace gases like nitrogen dioxide, bromine oxide, and tropospheric ozone (Rozanov et al., 2011; Ebojie et al., 2014). Using SCODA we have detected optically thin clouds throughout the free troposphere and very thin volcanic aerosol layer can be detected. Besides cloud top heights we also derived height resolved cloud occurrence frequencies to study global cloud field distributions.

In this study we used limb observations from the SCIAMACHY spectrometer to retrieve cloud top heights using the colour index ratio approach. We have investigated (a) the sensitivity of the method to detect clouds in SCIAMACHY limb measurements for different types of tropospheric clouds using the radiative transfer model SCIATRAN, (b) studied the latitudinal and seasonal variations of cloud heights, and (c) verified the method using comparisons to other satellite data and literature.

The paper is structured as follows. Section 2 provides information on the data being used in this paper. The method employed for the retrieval of cloud top heights from the limb scattered profiles is described in Sect. 3 and the influence of the limb path and the instrument's vertical field of view on the results is analysed in Sect. 3.1. In Sect. 4 model tests were performed with the radiative transfer model SCIATRAN to investigate the robustness of the method. Results from SCIAMACHY measurements are discussed in Sect. 5. The retrieval method is then validated with SCIAMACHY nadir data and MIPAS limb data in Sect. 6. The influence of aerosols on the retrieval is explained in Sect. 7 and conclusions are given in Sect. 8.

AMTD
8, 8295–8352, 2015

2 Data

2.1 SCIAMACHY

The atmospheric science instrument SCIAMACHY on board of ESA's ENVISAT was a high resolution 8-channel grating spectrograph (Burrows et al., 1995; Bovensmann et al., 1999). ENVISAT was launched on 1 March 2002 into a polar, sun-synchronous orbit. Contact to the satellite was lost on 8 April 2012. The SCIAMACHY instrument covered a spectral range from the UV-C (214 nm) to the near infrared IR-B (2386 nm), with a channel dependent spectral resolution between 0.22 and 1.48 nm. Scattered, reflected, transmitted, and emitted electromagnetic radiation was observed in solar/lunar occultation, Nadir-, and Limb-viewing geometry.

2.1.1 Limb data

Figure 1 gives an impression of the atmosphere from a limb viewing satellite perspective. The picture was taken from the International Space Station (ISS). The cloud patterns known from nadir viewing instruments are not detectable any more. Instead we see a strong increase in intensity from space towards the ground and a change of colour near the surface from dark blue to light blue/white, where we expect the influence of clouds.

The instantaneous field of view of SCIAMACHY at the tangent point was 2.6 km (VFOV) in vertical and 110 km (HFOV) in horizontal direction (across-track) for the nominal limb-scatter mode. The scanning of each tangent height took 1.5 s and four distinct measurements were normally made across-track. Each scene had a horizontal resolution of 240 km due to the scanning speed and integration time (Bovensmann et al., 1999) and the total swath was 960 km. The horizon was scanned in vertical direction from below the ground to about 92 km tangent height in more than 30 steps that are 3.3 km apart (Gottwald and Bovensmann, 2011). The atmosphere was undersampled with a vertical gap of roughly 0.7 km between two adjacent tangent heights. The

AMTD
8, 8295–8352, 2015

along track horizontal resolution is approximately 410 km for one VFOV shell, which will be explained in Sect. 4.1. The full Earth was covered after 6 days at the equator with better coverage towards the Polar Regions. Figure 2 gives a schematic view of the limb geometry. The red solid line depicts the instrumental line of sight (LOS) with the field of view (FOV) as red dotted lines. The blue numbered circles give the tangent heights of SCIAMACHY.

The main focus of the SCIAMACHY limb observations were daytime measurements of scattered solar radiation allowing retrievals of stratospheric O_3, NO_3, and BrO profiles. But also the retrieval of stratospheric aerosol extinction profiles and polar stratospheric cloud top heights was possible (von Savigny et al., 2005b). Night-time limb measurements were used to retrieve mesospheric temperatures (von Savigny et al., 2012).

We used the SCIAMACHY version 7.04W level 1b spectra. The level 1b data was calibrated without the polarization correction due to known problems in limb geometry (Liebing, 2013). The radiometric calibration was omitted as the colour index ratio is a division of two neighbouring tangent height measurements and thus no absolute calibration was needed. Height resolved limb-scattered spectra were taken from the instrument channels 4 (750 nm) and 6a (1090 nm) (von Savigny et al., 2005b).

Figure 3 shows the limb radiance I [photons s^{-1} m^{-2} nm^{-1} sr^{-1}] as a function of wavelength λ [nm] in the channels 4 and 6 for tangent heights ranging from 2.3 to 22 km. Not plotted are radiances measured in channel 5. Higher intensities can be seen in channel 6 when cloud scattering occurs. A steeper gradient between radiances from both channels is measured at tangent height 15.4 km compared to the lower height 12.1 km. This means that clouds are in the field of view at tangent height 12.1 km and scatter more radiance into the line of sight.

Spectral windows with molecular absorption bands, e.g. for ozone, oxygen, and water vapour, disturb the retrieval because of additional absorption features with a different height distribution. Radiation at wavelengths below 400 nm is not suitable because the

AMTD
8, 8295–8352, 2015

atmosphere gets optically thick in the upper troposphere due to Rayleigh scattering and ozone absorption increases towards the Hartley-Huggins bands.

2.1.2 Tangent height knowledge

The SCIAMACHY tangent heights are not fixed over time and vary up to 400 m along an orbit. Variations of up to 600 m are possible within a month. During the early phases of the SCIAMACHY mission the limb tangent height information was erroneous with differences between the estimated and the real tangent height up to several kilometres (Kaiser et al., 2004; von Savigny et al., 2005a). The main reasons for the tangent height differences are satellite attitude knowledge errors and a misalignment between the SCIAMACHY optical axes and the satellite reference frame, which were later identified and corrected (Gottwald et al., 2007).

The tangent height knowledge for the operational level 1 data version 7 is accurate within 50 m and no significant trends were found over mission lifetime (Bramstedt et al., 2012). Figure 4 shows averaged SCIAMACHY limb tangent heights of profile index number 3 and the corresponding 2-σ standard deviations (blue dashed), that were calculated from the first measurements of each orbit of one day at the beginning of each month. Overplotted is the difference between two adjacent tangent heights (red line). The step width between these two tangent heights is ≈ 3.3 km. The intra-annual variations were largest at the beginning of the mission in 2003 with tangent heights varying from about 6.8 km in spring to 4.7 km at the end of the year. This was the time when the limb measurements were fine-tuned. For the period until the end of 2010, we found an intra-annual cycle with an amplitude of about 150 m with lowest tangent heights at the beginning of the year.

The orbital height of the ENVISAT satellite has been lowered by about 17.4 km in October 2010 to extent the mission lifetime. As a consequence, each limb state was shortened by one tangent height step to maintain the limb/nadir matching. The limb tangent height pattern was modified in January 2011. The effect of these changes can

AMTD
8, 8295–8352, 2015

also be seen in Fig. 4 when tangent heights were lowered by roughly 100 m and the step width was slightly reduced (red line).

2.1.3 Nadir data

The Semi-Analytical CloUd Retrieval Algorithm SACURA (Rozanov et al., 2004; Kokhanovsky et al., 2005) retrieves the effective radius of cloud droplets, the liquid water path and other parameters like the optical thickness for optically thick clouds ($\tau \geq 5$). The cloud top height is determined from spectral measurements in the oxygen A-band (755–770 nm). Lelli et al. (2012, p. 1556, Fig. 1) showed that the total cloud top height error is about ±400 m for most cases. The CTH errors increase with cloud height and can be up to 1400 m for high clouds with a low optical thickness. It has to be noted that SACURA takes multiple scattering of light inside and below the clouds into account. The cloud top height retrieval is therefore more accurate than what can be expected from retrieval schemes treating clouds as Lambertian reflectors. Stubenrauch et al. (2012) showed that passive remote sensing techniques tend to detect a "radiometric cloud top height", which can be up to a few kilometres lower than the physical cloud top height.

2.2 MIPAS

The limb sounder MIPAS retrieved vertical temperature, trace gas profiles, and cloud distributions. The Fourier transform infrared (FTIR) spectrometer measured emissions in the mid-infrared ranging from 4150 to 14 600 nm with high spectral resolution (Fischer et al., 2008). While SCIAMACHY scanned the limb in forward flying direction of the ENVISAT satellite, MIPAS faced backwards. MIPAS had a similar resolution as SCIAMACHY in limb mode along the line of sight (LOS) and in vertical direction (3 km), but the resolution perpendicular to the LOS of 30 km is considerably higher than SCIAMACHY (240 km). Due to the specific spectral measurement range MIPAS is able to

AMTD
8, 8295–8352, 2015

measure day and night and as a pure limb sounder recorded more limb scans per orbit than SCIAMACHY.

After 2005 the nominal MIPAS mode was chosen as follows: the scan measurement time was 56.7 s with 27 floating altitude grid points from 7 to 72 km. The vertical sampling step size in the UT/LS region was 1.5 km. The lowest tangent height was not constant along an orbit, but changed from 5 km at the poles to 12 km at the equator as a function of latitude ϕ with $z_{\mathrm{th}}(\phi) = 12 - 7 \cdot \cos(90 - \mathrm{abs}(\phi))$ (Raspollini and Ceccherini, 2011). This has an impact on the comparisons as clouds top heights are not comparable below about 9 km in the tropics and extratropics.

Different methods to detect clouds have been developed for MIPAS (Spang et al., 2012). A fast detection scheme for the operational level 2 processing has been developed which is based on a cloud index (CI) method (Spang et al., 2002) to omit cloud-contaminated measurements. This method was also used to derive cloud field characteristics like global cloud top distributions and occurrence frequencies (Spang et al., 2005; Sembhi et al., 2012). The standard operational CI approach used two micro windows from 788.2 to 796.2 cm^{-1} and from 832.0 to 834.4 cm^{-1} in the MIPAS CI-A band. Sembhi et al. (2012) presented an optimised cloud and aerosol detection method for MIPAS in which new seasonal-, latitude- and altitude-dependent cloud detection thresholds were calculated to maximise the sensitivity to cloud/aerosol particles in the MIPAS field of view. Based on these thresholds, a MIPAS CTH dataset was calculated for the entire MIPAS mission and is used in this study.

3 Determination of colour index ratios and retrieval of cloud top heights

SCIAMACHY provides measurements of the limb scattered light integrated along the line of sight. When choosing wavelengths where trace gas absorptions and emissions can be neglected (e.g. around 750 and 1090 nm), the detected radiation of light is dominated by the scattering processes itself. These are Rayleigh scattering by molecules and Mie scattering by aerosol and cloud particles. Water and ice clouds show simi-

AMTD
8, 8295–8352, 2015

lar reflection characteristics in this wavelength range but start to differ at wavelengths larger than 1400 nm (Kokhanovsky et al., 2006).

Dividing the spectrally averaged radiances of two wavelength bands (750–751, 1088–1092 nm) by each other, we can differentiate measurements with particles in the FOV and those uncontaminated by particles. This is called the colour index approach. Colour is here defined as the ratio between radiances from two different wavelength bands of the same viewing LOS or tangent height. This technique was previously applied to limb measurements for the detection of polar stratospheric clouds from SCIAMACHY limb measurements (von Savigny et al., 2005b) and the determination of the cloud top height of a hurricane cell (Kokhanovsky et al., 2005). This work is a generalisation of these previous studies with respect to global particle (cloud) detection and the use of SCIAMACHY tangent heights from the Earth's surface up to 30 km.

The cloud top height z_{ct} [km] is determined using radiance profiles in different wavelength regions. The height-dependent colour index $CI(z_{th})$ is calculated for all tangent heights z_{th} [km] from the ratio of two limb scattered radiance intensities I at different wavelengths λ:

$$CI(z_{th}) = \frac{I_h(z_{th}, \lambda_h)}{I_l(z_{th}, \lambda_l)}, \quad (1)$$

where "h" denotes the high and "l" the low band. The radiances are spectrally averaged for the two bands 750–751 nm and 1088–1092 nm. For SCIAMACHY the maximum signal-to-noise ratios are of the order of 10 000 for both the low and the high band, so that noise is not an issue in these retrievals. The colour index ratio (CIR) Θ [–] can then be defined as:

$$\Theta(z_{th}) = \frac{CI(z_{th})}{CI(z_{th} + \Delta z_{th})}, \quad (2)$$

where Δz_{th} is the step width between two adjacent tangent heights $z_{th,i}$ and $z_{th,i+1}$. The tangent height grid of SCIAMACHY limb observations, i.e. the spacing between

AMTD
8, 8295–8352, 2015

adjacent altitude levels, is about 3.3 km wide (see red line in Fig. 4). The function $\Theta(z_{th})$ has a peak at the tangent height where the cloud top z_{ct} is within the field of view along the line of sight. If Θ exceeds the predefined constant threshold of 1.4, the cloud top is allocated to that tangent height. Due to the use of ratios the radiance calibration was not necessary as all multiplicative and height-independent calibration errors cancel out.

Figure 5a shows an example of the cloud index ratio profile for one SCIAMACHY measurement state (29 October 2006 10:16:10.63 UTC) over Europe. Four independent profiles situated across-track of the orbit were measured simultaneously. Clouds are detected, when the CIR Θ peaks and exceeds the threshold of 1.4 (dashed blue line). Depending on the atmospheric state, $\Theta(z_{th})$ is an unknown function of the cloud optical thickness, scattering geometry, albedo, aerosol loading, and the signal-to-noise ratio of the measurements. The sensitivity of Θ to the scattering geometry and optical characteristics will be discussed in Sect. 4. Figure 5b shows the colour index, which is a prerequisite product.

$\Theta(z_{th})$ can peak more than once in a profile, but we only store the highest peak and store this event in the quality flags accordingly. The double peaks occur in roughly 10 % of all retrievals, suggesting that two or more distinct cloud layers were detected. This can happen when a thin cloud is above a low thick cloud. When the highest cloud is optically thick, it is not possible anymore to separate cloud layers. The limb viewing geometry is not well suited to deal with layering of clouds as the position of a cloud along the light path is not known (see also Sect. 4.1).

3.1 Limb optical thickness

The biggest difference between nadir and limb cloud detection is the much larger limb path length and thus a much coarser horizontal resolution. Long pathways greatly enhance the sensitivity of the limb measurements. But looking sideways into a cloud field leads to information loss on the cloud fraction of the scene at the tangent point. Thus the retrieved cloud fractions will in general be much higher than what was found from Nadir measurements. This will be further analysed in Sect. 5.

AMTD
8, 8295–8352, 2015

The optical thickness τ_L of a cloud in limb viewing geometry is much higher than the vertical optical thickness τ_N due to the longer horizontal light path. This path length depends on the instrument's vertical field-of-view (VFOV) and the tangent height. For a cloud at 15 km tangent height that is covering the full VFOV of 1 km an increasing factor of 226 was calculated for the optical depth. Due to the curvature of the atmosphere, a cloudy layer will be outside the VFOV at a certain point along the line of sight. When taking the area made by the shell and the VFOV into account, we calculate an area weighted factor (AWF) of 151 for the example above. In general, a cloud will not cover the whole VFOV as a horizontal layer, so that this factor is the maximum increase that is possible. For SCIAMACHY with a VFOV of 2.6 km, we calculate an AWF of 243. But as e.g. thin cirrus clouds will not fill the VFOV completely, this factor is generally too high. Reducing the VFOV to 0.1 km to simulate this effect, we calculate an AWF $\approx$ 47. This is a more realistic value for the increase of the vertical optical depth due to limb geometry.

As a result, a subvisual cloud layer with an optical thickness $\tau_N = 0.025$ lying within the field of view of SCIAMACHY will give a limb τ_L of about 6 (AWF = 243) and about 1.2 for thin clouds (AWF = 47). In limb view, clouds are seen against the surrounding atmosphere and the background space. The contrast between a cloudy and non-cloudy part of the profile is high as the air mass above a cloud has less air and hence a lower scattering ability, so it will be darker (see the decrease of brightness towards outer space in Fig. 1). The nadir cloud detection is partly dependent on the contrast at the ground, e.g. ice or snow can lead to larger errors in the cloud optical thickness determination (Lelli et al., 2012; Lelli, 2013).

4 Model simulations

Simulating radiances in cloudy atmospheres is difficult (Kokhanovsky, 2001) because radiative transfer models like e.g. SCIATRAN (Rozanov et al., 2014) treat clouds only as two-dimensional layers with a defined vertical extent and general stratified physical

AMTD
8, 8295–8352, 2015

properties (optical thickness, effective radius of particles, phase function, cloud phase). This is of course a strong simplification of the complex three dimensional structure of a cloud.

We have studied the strengths and limitations of the fast and simple retrieval method to detect cloud top heights from limb measurements using model simulations of SCIATRAN. The software package SCIATRAN version 3.1.28 (Rozanov et al., 2014) was used to test the sensitivity of the retrieval method for typical atmospheric cloud scenarios. The influence of optical and geometrical cloud parameters (e.g. optical thickness τ, cloud top height, layer thickness) and the geolocation (sun zenith angle, relative azimuth angle) on the colour index ratio will be studied in this section. The forward model including cloud properties was described by Rozanov et al. (2014). A model accuracy of 5 % was found by Kokhanovsky and Rozanov (2003) for cloud optical thicknesses τ_N larger than 5.

SCIATRAN was already used for cloud sensitivity studies of the limb ozone retrieval (Sonkaew et al., 2009). The authors of the study concluded that the height range used for the retrieval of ozone profiles has to be limited to tangent heights above the cloud top in order to reduce retrieval errors. Cloud top heights can best be retrieved by using the same instrument and measurement mode of the trace gas retrieval. The cloud top height retrieval model SCODA has already been implemented in the SCIAMACHY level 2 version 5 operational processor in October 2010 (ESA, 2013).

As ENVISAT moves along the orbit on the day side from the north to south, the sun zenith angle (SZA) and the relative sun azimuth angle (SAA) are varying at the limb tangent point. The SAA is the angle between the line of sight and the sun beam. Because ENVISAT flies in a sun-synchronous orbit with a descending node crossing time of 10.00 a.m., only certain combinations of these parameters are possible. Naturally the highest sun zenith angles occurred near the poles and minima in the tropics (about 26°). The relative azimuth angle was generally lower towards the northern high latitude (about 22°) and largest at the southern high latitudes (about 157°). The Rayleigh scattering phase function minimum is at 90° and maxima occur in forward and back-

AMTD
8, 8295–8352, 2015

ward scattering direction. Scattering of light is highest in the north due to stronger forward scattering by aerosols and clouds at low azimuth angles. The minimum scattering occurs in tropical regions for SAAs larger than 90°. Table 1 shows typical angle combinations of the SCIAMACHY limb measurement geometry for one orbit from 29 October 2006.

The following parameters were chosen to test the sensitivity of the colour index ratio in a cloudy atmosphere. A spherical atmosphere with refraction was modelled with the radiative transfer model SCIATRAN. The scalar discrete ordinate technique was used to solve the radiative transfer equation. Absorption of the trace gases O_3, NO_2, and SO_2 was taken into account. The surface was modelled as a Lambertian reflector with a constant albedo $a_s = 0.1$, which is roughly twice as high as the albedo of water surfaces. The tangent heights were chosen from 0 to 30 km with a step width of 3 km. Wavelengths were taken from 750.0 to 751.0 nm with 0.2 nm step width and from 1088.0 to 1092.0 nm with 0.8 nm step width. The SZA was varied between 20 and 85°, and the SAA between 20 and 160°, which were roughly the maximum values that are possible for SCIAMACHY limb measurements (see Table 1).

To find the limitations with respect to cloud height and optical thickness, we simulated limb radiances for cloudy atmospheres. We have used a water cloud layer situated between 4 and 5 km, that has a spectrally dependent optical thickness of $\tau_{N,\mathrm{wc}}$=1 at 500 nm, which is considerably lower than the global cloud optical thickness of 3.7. The radius of the water droplets was assumed to be 10 µm, which is in the range of values from literature (Rossow and Schiffer, 1999). Also a cirrus cloud layer was simulated being made of hexagonal ice crystals with 100 µm height and 50 µm side length. The layer optical thickness of $\tau_{N,\mathrm{ic}} = 0.01$ was assumed, which is in the sub-visual range. The cloud layer was inserted between 14 and 15 km. In general, ice crystals can substantially range in size from 10 to about 2000 µm and exhibit a variety of different shapes (Liou, 2005).

The influence of aerosol contamination on the cloud retrieval was taken into account. We used the LOWTRAN aerosol parameterization defining the height depen-

AMTD
8, 8295–8352, 2015

dent extinction coefficient and single scattering albedo. A total aerosol optical thickness $\tau_{N,a} = 0.14$ at 790 nm and 0.116 at 1090 nm was selected, which is in the range of values measured over oceans (see e.g. Boucher et al., 2013, Fig. 7.14). Phase functions were calculated using the single parameter Henyey–Greenstein analytical formula with an asymmetry factor of 0.772 (0.0–4.0 km), 0.669 (4.0–10.0 km), and 0.657 (above 10.0 km).

In Fig. 6 calculated colour index ratios are shown as a function of sun azimuth (SAA) and sun zenith angles (SZA). The step size was 5° in SZA and 10° in SAA direction. The calculations were made for (a) a low, thick water cloud (4–5 km, $\tau_{N,wc} = 1$) and (b) a high, sub-visible ice cloud (14–15 km, $\tau_{N,ic} = 0.01$). Overplotted in black dots are typical SAA/SZA combinations of the SCIAMACHY limb tangent point along a typical orbit. Cloud tops were in general detectable for all SZA/SAA pairs, because the modelled Θ exceeds the threshold of 1.4. The water cloud CIR was highest for very low SAA ($\Theta > 2.0$) and lowest around 90° SAA ($\Theta < 1.6$), which is in the tropical region. The reason of this change can be attributed to the form of the phase function of water droplets peaking in forward direction. Because of the phase function asymmetry we found the lowest CIR values for water clouds in backward direction of the scattered light beam (South Polar Regions), where the threshold was not reached (see Table 1). The phase function of an ice particle is more complex and has a stronger asymmetry. Thus we retrieved a more pronounced CIR dependence due to SAA changes with lowest values below 1.8 around 140° S. Moreover even for high SAA/SZA values we found high CIR.

The modelled CTH can correctly be retrieved for clouds tops of 5 km and higher. But a CTH at 3 km was not detectable in this test case, as the modelled aerosol loading (optical depth of roughly 0.125 between the ground and 5 km at 790 nm) lead to a shift of the retrieved CTH to the next higher model tangent height and also reduced the CIR. Most of the aerosols are within the first 5 km. But it is possible to retrieve the correct CTH, when the modelled aerosol loading was reduced to 25 % of the original value (i.e. $\tau_{N,a} = 0.035$). The retrieved Θ for a water cloud ($\tau_{N,wc} = 1$) between 2 and 3 km

AMTD
8, 8295–8352, 2015

was then above the detection threshold between 1.4 and 1.6 for nearly all geometry combinations. Simulating an ice cloud (here $\tau_{N,\mathrm{ic}} = 1$) at the same height, it was already possible to retrieve the correct CTH for aerosol loadings of about 40 % of the modelled aerosol optical thickness ($\tau_{N,\mathrm{a}} = 0.05$). So clouds at the lowest SCIAMACHY tangent height above the ground at about 2–3 km can only be detected for a very low aerosol loading. These low aerosol optical depths can be found in clean areas over oceans especially in the Southern Hemisphere.

The influence of CTH changes on the CIR Θ was also tested. A water cloud ($\tau_{N,\mathrm{wc}} = 1.0$) of 1 km thickness was shifted from 3 to 18 km. The retrieved Θ was strongly increasing towards higher heights from about 1.6 (5 km) to 3.1 (18 km). So the retrieval sensitivity was sufficient at lower tangent heights and increased with height. Furthermore, clouds were detectable for an optical thickness of 0.1 at the lowest tangent heights and for 0.005 in the upper troposphere. These values are calculated for spherical shell cloud layers and can be interpreted as theoretical lower limits which in reality might not be reached, as a very thin cirrus cloud field has a limited vertical and horizontal extent.

The tangent heights stored in the SCIAMACHY level 1C data are geometric ones, where refraction was not taken into account. The refractive effect that lowers the real tangent height is negligible above 22 km, when differences between geometric and refracted tangent heights are less than 100 m. But at z_{th}=6 km, the real light path has a refracted tangent height of about 4.9 km. Furthermore the vertical field of view increased due to the refraction. The lower edge of the geometric VFOV was at 4.7 km and the upper one at 7.3 km. The corresponding refracted VFOV edges are then at 3.4 and 6.4 km, respectively. This means that the refractive VFOV is about 3 km wide. The VFOV at the lowest geometric tangent height of 2.3 km will already include the surface. So we might be able to detect clouds down to the Earth's surface with the restriction that at these heights the colour index ratio is near the threshold and also very sensitive to aerosol contaminations that increase towards the surface.

AMTD
8, 8295–8352, 2015

Sub-visible ice clouds in the upper troposphere are clearly detectable. For a tropical upper tropospheric cloud (SZA = 25°, SAA = 83°, cloud layer 15–16 km) the cloud detection threshold was already exceeded for cloud optical thicknesses τ_N of about 0.003. Here the influence of aerosols and refractive tangent height changes are negligible. But the cloud retrieval can be obstructed by intrusions of aerosols into the upper troposphere from volcanic activity, when the optical thickness of cloud and aerosols has the same order of magnitude.

4.1 Horizontal Sampling

The along-track horizontal sampling for one atmospheric shell $2x(i,i)$ is about 410 km, where i is the index of the tangent height $z_{\mathrm{th}}(i)$ (see Fig.2). But the cloud position within this shell cannot be resolved with this retrieval technique. So the real length, where clouds can be sampled, is much longer, as they may also appear in the line of sight outside the lowest shell given by $z_{\mathrm{th}}(i)$. The tropopause is the upper edge where clouds exist under normal conditions. This can be as high as 17 km in the tropics. Using this tropospheric boundary height (index i_{tp}), we can calculate the cloud top height dependent extra path length. For a cloud top at z_{th} = 6 km in the tropics, we find a nearly doubled total horizontal sampling length $\sum x(i, j = i, \ldots, i_{\mathrm{tp}})$ of 790 km and for a 12 km cloud top the extra path is 150 km, where clouds can be inside the VFOV. So when a cloud top of z_{th} of 3 km was detected e.g. over Germany, the cloud could be anywhere along the countries North/South axis (about 800 km) at altitudes up to the tropopause.

It should be noted that this horizontal sampling length is in the order of distance between two consecutive SCIAMACHY limb measurement states. The geographic angle is about 7° (e.g. the latitude) between two SCIAMACHY states. For most of the cases the LOS above a cloud top in one state will not reach the area of an adjacent state as it leave the troposphere before. But if the LOS of a cloud free pixel has a tangent point close to the surface, the along track horizontal resolution is in the order of 1200 km corresponding to an angle of roughly 10°.

AMTD
8, 8295–8352, 2015

To check if these long extra paths are relevant for the cloud detection, we also have to take the vertical resolution into account. We have calculated the vertical area-of-sight a [km^2], that the line-of-sight crosses in each shell segment because of the instrumental field of view. The results are independent of the across-track LOS. For example, the path length ratio $x(3,3)/x(3,4)$ is roughly 2.4 and the corresponding ratio between two adjacent areas $a(3,3)/a(3,4)$ is only 1.2 (see Fig.2). So the areas differ not very much and thus the influence from the outer shell areas on cloud detection is not negligible.

In trace gas limb retrievals, number densities are calculated for each shell assuming a horizontal continuity in each shell. So it is possible to derive a trace gas profile at the tangent height. This is not possible for discontinuous cloud fields. If e.g. the area $a(3,3)$ is free of clouds and $a(3,4)$ not, the retrieved CTH will be higher in this case. These high clouds outside the along-track FOV or lowest shell can lead to a CTH overestimation and will also increase the cloud fraction.

5 Results

In this chapter results of the SCODA retrieval are presented. We retrieved annual means of cloud top heights and fractions for all tropospheric tangent heights. Limb cloud fractions were calculated by counting the number of cloudy pixels within a grid cell.

5.1 Annual average cloud top heights and fractions

Figure 7a shows the annual averaged cloud top height [km] of 2006, gridded on a $2^\circ \times 2^\circ$ map. All measurements of that year (roughly 445 000), that exceeded the threshold of $\Theta = 1.4$, were used to make the mean. Overplotted in Fig. 7a is the size and distance of three typical SCIAMACHY limb scan cycles (red rectangles). Four simultaneous measurements in across-track direction were made. This is illustrated in Fig. 7b, where a zoom into one rectangle that has the lower left corner at the equator over

AMTD
8, 8295–8352, 2015

the Gulf of Guinea was shown. A cloud image (Reuter and Pfeifer, 2011) from SEVIRI (Spinning Enhanced Visible and Infrared Imager) aboard Meteosat is shown to visualize the fine structure of a nadir cloud field within a limb scan. In general, the horizontal cloud structure is not detectable in limb view, as a large volume is scanned and only the highest cloud tops contribute to the limb result in that area.

The highest clouds (from about 13–16 km) were detected in the tropics. These are deep convective and cirrus clouds. The lowest clouds are found in the Southern Hemisphere west of the continents (about 4 km). Also a stream of relatively high clouds is detected ranging from the Caribbean Sea over the North Atlantic Ocean towards Northern Europe. This can be related to extra-tropical storm tracks. Similar features are found east of Japan and in the South Pacific Ocean towards the west coast of South America. An interhemispheric CTH difference was also observed, which will be analysed later.

We also found the interhemispheric difference in the CIR annual average in Fig. 8a. Especially for latitudes above 60° N/S, the CIR differed roughly by about 0.4. This is partly due to dependence of the phase function on the viewing geometry, as was shown in Sect. 4. The SAA ranges from 30° (NH) to 150° (SH) at these latitudes where we also detected CIR differences from model studies (see Fig. 6a). Low CIR regions were furthermore detected in low cloud top height areas, which is in line with our expectations from model studies.

Figure 8b shows the limb cloud fraction. All measurements flagged as cloudy were counted if the cloud top height was above the ground and below 19.9 km. You can see much higher values in comparison to cloud fractions retrieved in nadir geometry. Because of the long viewing path through the atmosphere more than 90 % of all measurements are marked as cloudy and the difference between both Polar Regions is rather small. Only at low cloud tops in the Southern Hemisphere, west of the continental coasts, we also found comparatively low cloud fractions of about 70 %. Because of the long tropospheric geometric path length of 1200 km, cloud free pixels in SCIAMACHY limb measurements were detected only rarely. Spang et al. (2012) called this

AMTD
8, 8295–8352, 2015

the “limb-smearing effect”, which makes comparisons to nadir measurements complicated. We did not expect a high cloud coverage over desert areas like Australia and North Africa, but found a significantly higher cloud fraction e.g. over North Africa in comparison to measurements from high resolution nadir instruments. This can be attributed to measurements of desert dust blown away from these areas at heights up to 6.5 km (see Fig. 9a–b) and to cirrus clouds at higher altitudes, that are not detectable by passive nadir instruments.

5.2 Height resolved cloud fraction

Figure 9 shows the annual mean cloud fraction [%] of 2006 for all SCIAMACHY limb tangent heights in the tropospheric region. The limb cloud fractions are divided into 6 height regions covering those nearly constant tangent heights (over time and space). The fractions are calculated by comparing the number of clouds in that layer with the number of all measurements. Clouds are limited to the troposphere, but polar stratospheric clouds (PSC) are generally being found above 18 km (von Savigny et al., 2005b). Furthermore, volcanic eruptions can transport material into the stratosphere that can be detected with the colour index method, which will be discussed in Sect. 7.

For the layer 1.0–3.75 km the highest amount of low clouds was retrieved over oceanic regions in the Southern Hemisphere westwards of the continents (Fig. 9a). Slightly more clouds were detected overall between 1.0 and 6.5 km in the South Polar Regions than in the northern ones. It seems that the method is rather insensitive to low clouds for low scattering angles at high northern latitudes. The elevated cloud levels over North Africa might be due to aerosols uplifted by dust storms over the Sahara, as this region is normally nearly cloud free. High fractions were also detected at the height range (Fig. 9b). Generoso et al. (2008) measured dust plumes from Africa up to 8 km altitude over the Atlantic. High CF from the mid-latitudes to the Polar Regions were also detected by CALIPSO (Chepfer et al., 2010, see e.g. Fig. 3g–h). Larger CF for low clouds (CTH < 3 km, > 680 hPa) were detected in their study mainly over the oceans, especially near the west coasts of the continents, which is in line with our findings

AMTD
8, 8295–8352, 2015

in Fig. 9a. But CALIPSO detected no enhancement of cloud fractions over Northern Africa, which indicates that SCIAMACHY possibly detected an enhanced aerosol layer in this region.

The layer 6.5–10.0 km in Fig. 9c shows from where the interhemispheric CTH differences mainly originate. The cloud fraction in the northern hemisphere at latitudes higher than 30° is 50 % and more, while in the Southern Hemisphere it is less than 40 %. At the next layer above 10 km cloud tops are found in areas of frequent storm activities in the extra-tropical zone above 30° N/S (see e.g. Atlas of Extratropical Storm Tracks, available at: http://data.giss.nasa.gov/stormtracks/). These regions are also detected in CALIPSO high level clouds above 7.2 km (Chepfer et al., 2010, Fig. 3c–d).

The occurrence of clouds above 13.5 km is limited to the tropical zone as displayed in Fig. 9e–f. Largest cloud fractions of about 70 % are detected over the western part of the Pacific from Indonesia to the East between 90 and 180° longitude. But high clouds are also detected over Central Africa and Middle America (above 40 %). Another feature is the slightly enhanced cloud fraction over Antarctica, which is due to the measurement of PSC in the southern winter/spring season. The PSC season is limited to a few months around September. The combination of cloud fraction patterns of all these layers explain the interhemispheric CTH differences seen in Fig. 7.

5.3 Temporal Evolution of CIR and CTH

The global colour index ratio changed slightly over time as shown in Fig. 10. After a rather stable period from the start until 2006 with CIR values above 2.0, the CIR has decreased down to 1.84 at the beginning of 2007 and then remained at values around 1.9 until the August 2011, where the largest decline down to 1.75 occurred. Some of these short-time CIR reductions correspond to the major volcanic eruptions in 2008, 2009, and 2011. This is expected as the lower stratospheric volcanic aerosol layers are optically very thin and the corresponding CIR is lower than for typical tropospheric clouds. Two other wavelength pairs were tested. The 1551/1090 nm CIR showed similar features. During the longer decontamination phases of the instrument

AMTD
8, 8295–8352, 2015

in August/December 2003, June/December 2004, and December 2008 the CIR was also reduced. The 1685/1551 nm CIR on the other hand was rather stable over time. This indicates that the ratio is not affected by aerosols as much. A CIR decrease over time might reduce the sensitivity to both very thin cirrus clouds and low altitude clouds, because we have used a temporally constant detection threshold of 1.4.

Time series of the SCIAMACHY CTH zonal monthly means are shown in Fig. 11a for latitudes between ±80°. The seasonal cycle and interhemispheric CTH differences can be identified. Higher CTHs were detected in the summer seasons of each hemisphere. Three volcano eruptions leading to deviations in cloud top height were found (see Sect. 7). Also the PSC season in the Southern Hemisphere winter was regularly measured, where the top heights lie in the stratosphere above 12 km. In the northern Polar Region the PSC season is not as clearly visible in the zonal means except for the winter season 2010/2011 (Hommel et al., 2014). In Fig. 11b the standard deviation (SD) is shown. Here the northern PSC were also easily traceable in the winters of 2005, 2007, and 2008.

There are other features both in CTH and standard deviation that cannot be attributed yet and need to be further analysed. A considerable increase in CTH was found starting at the end of 2007 around 20° N which has a large longitudinal scatter when taking the standard deviation in Fig. 11b into account. This might be originating from the volcano Tavurvur (4° S, 152° E) which erupted between August 2006 and January 2007 with a Volcanic Explosivity Index (VEI) of 4. Sulphur dioxide and ash clouds reached the tropopause in October 2006 and spread afterwards Northwest and Southeast (Global Volcanism Program, 2006). The largest CTHs were measured at the end of 2011 in the latitude band 0–10° N, which was accompanied by a large longitudinal scatter. Mean CTHs up to 21.3 ± 8.2 km were detected in December 2011, while normal values are in the order of 13 ± 4 km at this location and time of the year. So far the reason for this phenomenon is unclear. It might be attributed to rising aerosol particles after the Nabro eruption in June 2011.

AMTD
8, 8295–8352, 2015

6 Validation with SCIAMACHY nadir and MIPAS limb cloud top heights

The comparison of limb measurements with nadir retrieved cloud parameters is no simple task due to long light paths as discussed in Sect. 4 and also addressed by Spang et al. (2012). We first compare cloud top heights retrieved from the two viewing geometries nadir/limb of SCIAMACHY and interpret the differences. In the second subsection we validate our results with collocated limb CTH from MIPAS.

6.1 Comparison with SCIAMACHY nadir data

A perfect agreement between limb and nadir cloud top measurements cannot be expected. The two main limiting factors are the low geometrical limb resolution and the high optical thickness threshold of the nadir retrievals at least for passive instruments like SCIAMACHY. Figure 12 shows annually averaged cloud top heights [km] from SCIAMACHY nadir data calculated with SACURA (Lelli et al., 2014), where the corresponding 1-σ standard deviation of each grid cell has been added. This was done to minimize differences, as in limb only the highest CTHs are detected in a grid cell. Only data were used for the following SACURA quality checks: top height convergence (flag 2), top/bottom height convergence (5), high geometrical thickness (3), and a cloud optical thickness larger than 30.

Mapping SACURA data in this way, the agreement to limb cloud heights is generally good and the global cloud patterns are similar. But a higher land/ocean contrast was found in the nadir data which was blurred in limb data. Very high limb CTHs over South America and South Africa were only partly seen in nadir data. On the other hand the high nadir clouds over the Tibetian Plateau and the Andes were not detected in limb data. Also nadir CTHs over Australia were higher. The nadir standard deviation, which is not shown here, is in the order of 2–4 km. It was highest over the tropical oceans, where e.g. a scatter of up to 5 km was found over the Indian Ocean and the western part of the Pacific Ocean in the tropical belt. Nadir cloud tops were rather low (< 4 km) on the west coasts of South America, Africa, and Australia with a low scatter of less than

AMTD
8, 8295–8352, 2015

2 km. Although being at the SCODA detection limit, these low cloud tops are detectable in the limb retrieval at about 4 km.

Without the added standard deviation, nadir CTHs were systematically and globally lower. This is due to the fact that (a) the nadir retrieval is restricted to the detection of water clouds with an optical thickness of $\tau > 5$ and (b) the limb retrieval is not sensitive to very low clouds. But as the global optical cloud thickness is approximately 3.7 ± 0.3 (Rossow and Schiffer, 1999), a large amount of thin clouds cannot be detected by nadir passive sounders, e.g. high altitude cirrus clouds. This will consequently lead to a lower mean top height in the tropics where most of the cirrus clouds occur. But CALIPSO as an active nadir viewing instrument is able to detect thin clouds. Sassen et al. (2009) reported that 56 % of the total cirrus were found at subtropical latitudes of ±30°.

The latitudinal differences between limb and nadir CTH are summarized in Fig. 13, where SCIAMACHY zonal mean cloud top heights averaged over 7 years (2003–2009) are shown. The black line and the blue area depict the SACURA nadir results and its 1-σ scatter. The average CTHs are generally below 10 km in the tropics and decline to about 4 km towards the Polar Regions. The difference to the SCODA limb averages (orange line) is generally high. Limb CTHs were found to be up to 4.5 km higher in the tropics near 10° N. Lower differences of about 2 km were seen towards the South Polar Region. If the scatter is used to find the highest nadir clouds, we still measured differences of roughly 2 km in the tropics and of up to 2 km at latitudes above 40° N. The interhemispheric asymmetry is more pronounced in the limb measurements. If the years of high volcanic activity 2008 and 2009 were excluded from the limb average (blue dashed line), the cloud heights in the northern hemisphere were only slightly reduced by roughly 0.5 km in the latitude band from 20 to 82° N .

6.2 Validation with MIPAS limb data

Better agreement can be achieved with other limb viewing instruments that have a similar field of view and sensitivity to thin cirrus clouds and aerosol particles. Co-located SCIAMACHY and MIPAS limb measurements of cloud/aerosol top heights are com-

AMTD
8, 8295–8352, 2015

pared for this study. The average displacement of the limb tangent points from both sensors was in the order of 170 km and the temporal displacement was 800 s. We have used a MIPAS verification dataset with measurements from January 2008 to March 2012. Figure 14 shows a scatter plot of SCIAMACHY versus MIPAS cloud top height measurements for April 2010. The atmosphere was divided in six latitude bands spanning the whole globe for the colour coding. Overplotted is the SCIAMACHY vertical resolution of about 3.3 km. As MIPAS has a smaller tangent height step size and the tangent heights are varying continuously over a month, we do not see the gaps in vertical direction of the SCIAMACHY cloud top heights.

MIPAS detects the cloud tops in general slightly higher than SCIAMACHY. This is best observable for the SCIAMACHY tangent height at about 9 km. But there is also a higher percentage of MIPAS top heights that clearly lie outside the vertical field of view depicted by the dotted line. Most of these CTHs with the largest deviations were found in the tropics (yellow and green dots). This is the region where the lowest possible MIPAS tangent heights were at about 10 km, which can partly explain the differences. On the other hand, MIPAS has a smaller horizontal field of view across track, which limits the smearing effect to some extent.

Figure 15 summarizes the global CTH differences of SCIAMACHY and MIPAS. Results were zonally and monthly averaged. The vertical differences are around −1.1 km, which is in the range of the vertical field of views of both instruments that limits the vertical resolution. This difference can be mainly attributed to the different tangent height step sizes of 3.3 km for SCIAMACHY and 1.5 km for MIPAS. The largest differences and 1-σ standard deviations between both datasets are found at times of volcanic intrusions into the UT/LS region. Sembhi et al. (2012) compared MIPAS top heights with HIRDLS (High Resolution Dynamics Limb Sounder) and CALIOP (Cloud-Aerosol LIdar with Orthogonal Polarization) measurements and found that MIPAS CTHs are in the range of up to 1 km higher for altitudes between 12 and 20 km, which is in line with our comparisons.

AMTD
8, 8295–8352, 2015

Taking a closer look at the height resolved CTH differences, we found the highest discrepancies at the lowest tangent height used in the comparisons of about 8.7 km. In April 2010 the vertical displacement was -1.9 ± 1.3 km (415 collocations), -0.7 ± 1.7 km (1302) at 12 km, -1.1 ± 1.2 km (1071) at 15.3 km, and $+0.8 \pm 0.7$ km (128) at 18.5 km. Results from the lowest tangent height should be taken with caution, as MIPAS has latitude dependent tangent height cycle. Higher cloud top heights compared to MIPAS were found in general at the highest SCIAMACHY tangent height 18.5 km. This can partially be explained by the coarser tangent height step size of SCIAMACHY, as the 18.5 km height is generally above the tropopause. The largest differences at this height occurred during periods of volcanic aerosol intrusions. 1.9 ± 1.2 km difference (168 measurements) was calculated in October 2008 and 1.7 ± 1.5 km (245 measurements) in July 2009. MIPAS was also sensitive to volcanic aerosol particles at heights above the tropopause, where both instruments detected particles above 19.5 km in 2009, but in this case the difference of 4.0 ± 3 km was larger than their combined vertical FOVs. This suggests that the instruments have a different sensitivity to the sulphuric acid droplets in the lower stratosphere. The number of co-located measurements in September 2009 at the 18 km height (514) was more than 10 times higher than e.g. in 2010 (64).

In the second half of 2011 both instruments detected unusually high cloud/aerosol layer heights in the tropics (see Fig. 11). While in September 2011 the top heights around 18 km nicely agree (0.6 ± 0.8 km), the disagreement at the lowest tangent height was very large (-5.3 ± 2.6 km). The Nabro volcano injected large amounts of sulphur dioxide into the upper troposphere starting in June 2011 which was comparable to the Sarychev peak eruption 2009. It has to be noted that the very high CTHs at the end of 2011 were only detected with SCIAMACHY. But also MIPAS measured higher clouds on average during this period.

Furthermore we have compared zonal mean CTH for clouds between 6 and 28 km for three month averages in March-April-May and September-October-November 2003 with literature results from Spang et al. (2012, Fig. 12). The agreement was also good

AMTD
8, 8295–8352, 2015

with maximum differences of about 1.5 km. Moreover, not taking SCIAMACHY cloud top heights below 6 km into account, the interhemispheric CTH differences in the SCIAMACHY data had disappeared.

7 Particle detection due to volcano events

The influence of aerosols on the colour index ratio Θ has already been studied by von Savigny et al. (2005b). It was shown that high aerosol loading in the upper troposphere/lower stratosphere can lead to false polar stratospheric cloud detection. This is also true for the general retrieval of cloud top heights throughout the troposphere.

The lower the cloud top height, the more an aerosol layer can disturb the retrieval as the CIR Θ is strongly height dependent. Because of the lower values of Θ towards the surface the extra scattering due to aerosols have a high impact. Nevertheless, we detect CTH at the lowest tangent heights mainly in oceanic areas and to a higher percentage towards the South Polar Regions (see Fig. 9a). But as shown in the cloud fraction distributions, aerosols were influencing the detection over desert regions. Furthermore the intrusion of aerosol particles into the stratosphere is easily detectable even for a very low aerosol optical thickness. The same thresholds of τ_N apply to aerosols as were found for sub-visual cirrus.

There were three main events during the life cycle of SCIAMACHY, where volcanoes in the Northern hemisphere ejected a moderate amount of material into the lower stratosphere. These were falsely detected as clouds in the lower stratosphere for several months on a semi-global scale. Those were the eruptions from Kasatochi (52.1° N, 175.3.2° W) starting on 7 August 2008, Sarychev Peak (Matua Island: 48.1° N, 153.2° E) on 12 June 2009, and Nabro (Eritrea: 13.4° N, 41.7° E) on 13 June 2011.

The volcanoes emitted sulphur dioxide into the troposphere which was then transported towards the UT/LS region. Over time it was oxidized together with water to sulphuric acid and then condensed into larger droplets. This mechanism is slow and takes weeks for the transformation. The sulphuric acid droplets were then advected

AMTD
8, 8295–8352, 2015

around the globe. Due to the increasing particle diameter they were detectable with the SCODA method, as the optical depth was high in the UT/LS region. The EARLINET lidar site found aerosol optical depths at 532 nm between 0.004 and 0.025 in 2008 for heights above 5 km (Mattis et al., 2010) and up to 0.07 in 2009 (Kravitz et al., 2011). Mateshvili et al. (2013) measured optical depths up to 0.008 in July 2011 at a wavelength of 780 nm and a top height of the aerosol layer at 19 km was found. OSIRIS measured similar values and the aerosol layer was still detectable in the middle of September 2011 (Bourassa et al., 2012).

The main components in the Kasatochi and Sarychev ejections were sulphate (more than 50 %) and carbonaceous material (less than 43 %) (Andersson et al., 2013). These percentages changed over time in the UT/LS region. A residence time of 45 ± 22 days was estimated for both volcanoes from their measurements. Residence times in the UT/LS region are the longest for aerosols with particle diameters around 1 µm. But a large spread of residence times from 9 to 62 days was reported in other studies (Andersson et al., 2013).

The influence of stratospheric particles on the CTH detection was already seen in Fig. 11. Here we take a closer look at the impact of the three big eruptions and their temporal evolution on the CTH retrieval results. The measurements were sometimes dominated by aerosol particles in the lower stratosphere as was displayed by the red dots in Fig. 11 giving the latitude and estimated start of the breakout from the three volcanoes described above.

Figure 16 shows how high aerosols were transported into the lower stratosphere at latitudes between 30 and 70° N. For this latitude band the lowest layer of 12.5–15.5 km (red line) is situated in the UT/LS region. For latitudes near 30° N the layer is at the upper edge of the troposphere and towards 70° N in the stratosphere. Under normal conditions the highest occurrence frequencies occurred in summer seasons with maxima of nearly 5 % in the lowest layer. The year 2010 was an example of such an undisturbed year in contrast to the other years. So only a small amount of clouds were detected in the lowest layer and the two layers above were completely free of

AMTD
8, 8295–8352, 2015

particles for most of the year. Particles above 18.8 km were also found in the winter time PSC season.

Most of the particles were detected in the lowest layer between 12.5 and 15.5 km during the volcanic eruptions. In October 2008 up to 30 % of the area was covered with aerosols. In September 2009 the maximum coverage was about 48 and 17 % in August/September 2011. The second peak detected in September 2009 might be due to sedimentation of particles from the layer 15.5–18.8 km, which had the peak occurrence rate already in August (29 %). But still a considerable amount of aerosols were detected in the intermediate layer with maxima of 19 % in September 2008, 29 % in August 2009, and 23 % in August 2011. A pronounced occurrence frequency maximum of the layer 18.8–22.2 km was only found in September 2009 (10 %) with lower frequencies in the months before and after September. Overall about 45 % of all measurements in the lower stratosphere were made in October 2008, 82 % in August 2009, and 40 % in July 2011.

The duration of elevated aerosol levels was about 4 months in 2008, 7 months 2009, and 5 months 2011. The measured time spans of the aerosol layer detection in 2008/2009 is in line with measurements from IASI of H_2SO_4 (Clarisse et al., 2013) and OSIRIS for both volcanoes (Bourassa et al., 2010; Haywood et al., 2010). ACE-FTS measurements of SO_2 and sulphate aerosols gave a lifetime of the Sarychev particles of about 7 months (Doeringer et al., 2012). They detected the plume between 8.5 and 17.5 km with a maximum around 12 km at higher latitudes (55–70° N).

While the volcanoes Kasatochi and Sarychev Peak are at similar latitudes in the Northern hemisphere, the Nabro volcano is in the tropics and the particles had to be advected into the Northern region over time. This might explain why we found higher amounts (23 %) of particles in the layer 15.5–18.8 km (August 2011) than in the layer below, as the particles were already vertically transported into the lower tropical stratosphere and then have been moved northwards, where they descended again.

AMTD
8, 8295–8352, 2015

8 Conclusions

SCIAMACHY limb measurements were used to investigate the global cloud top height and occurrence distributions for the lifetime of the instrument. This was done using a colour ratio method, which was already successfully applied to nadir retrievals and the detection of PSCs in limb view. Although the use of only one threshold for all atmospheric situations is simplistic in nature, it was shown that it was sufficient for the majority of cases, except for the lowest clouds. For low tangent heights between 2 and 5 km the influence of aerosols and viewing geometry is not negligible and can lead to wrong results because the retrieved cloud top height could be shifted towards the next tangent height. But in clean areas mainly over southern oceans we were able to detect low clouds at heights between 2 and 5 km. This was supported by comparisons with nadir measurements of SCIAMACHY.

SCIATRAN model studies have shown that the method is very sensitive for a wide range of cloud optical properties and cloud top heights. But due to coarse spatial resolution, the vertical accuracy of the CTH retrieval is limited to the tangent height step size of about 3.3 km. The wide horizontal field of view of about 800 km along-track and 240 km across-track also promoted smearing effects with respect to the location of the cloud field. But comparisons of four years of co-located MIPAS data, which has a narrow 30 km across-track FOV and a tangent height step of 1.5 km, have shown good agreement. SCIAMACHY CTHs were generally lower by about 1 km, which can be explained by differences in the tangent height steps.

The influence of aerosols was not only problematic at low tangent heights in polluted areas but also after large intrusions of sulphuric acid droplets and ash particles from volcano eruptions into the UT/LS region. We detected large aerosol contaminated areas for long periods of several months mainly in the northern hemisphere. In 2009 after the Sarychev volcano eruption the northern stratosphere was loaded with particles from the poles down to the extra tropics for nearly 7 months. Particles were detected up to heights of about 22 km.

AMTD
8, 8295–8352, 2015

We analysed monthly-sampled cloud top altitudes measured by SCIAMACHY for the two different observational geometries limb/nadir. It was shown that the height differences can partly be attributed to the different sensitivities of the viewing geometries. To this end, a Limb-Nadir matching technique would prove to be advantageous in filling the gaps of representation of specific cloud types/regimes which can be seen in only a viewing geometry and not in the other. Unfortunately, SCIAMACHY was the only instrument so far that was capable of making use of the two viewing geometries.

The cloud top height detection method was first used to detect PSCs and later updated into the algorithm SCODA to improve the operational limb trace gas retrievals towards the tropopause. It has now also proved its validity for cloud and aerosol studies. The use other wavelength pairs in the near IR, which is not discussed here, enables to distinguish between clouds and aerosols. Although both SCIAMACHY and MIPAS have proven to be of great value for studies in the UT/LS region because of their high sensitivities, instruments with limb viewing capabilities for replacement are not foreseen at the moment.

Acknowledgements. This work was funded in part by ESA within the SCIAMACHY Quality Working Group (SQWG) project and the Sentinel5-Precursor L2 development project (DLR grant no. 50EE1247). The work was supported by the European Space Agency (ESA), the German Ministry of Education and Research (BMBF), the German aerospace centre (DLR), the University of Bremen and the Ernst-Moritz-Arndt University of Greifswald, Germany. SCIAMACHY was jointly funded by Germany, the Netherlands and Belgium.

The article processing charges for this open-access publication
were covered by the University of Bremen.

References

Andersson, S. M., Martinsson, B. G., Friberg, J., Brenninkmeijer, C. A. M., Rauthe-Schöch, A., Hermann, M., van Velthoven, P. F. J., and Zahn, A.: Composition and evolution of volcanic aerosol from eruptions of Kasatochi, Sarychev and Eyjafjallajökull in 2008–2010 based

AMTD
8, 8295–8352, 2015

on CARIBIC observations, Atmos. Chem. Phys., 13, 1781–1796, doi:10.5194/acp-13-1781-2013, 2013. 8325

Boucher, O., Randall, D., Artaxo, P. Bretherton, C., Feingold, G., Forster, P., Kerminen, V.-M., Kondo, Y., Liao, H., Lohmann, U., Rasch, P.,Satheesh, S. K., Sherwood, S., Stevens, B., and Zhang, X. Y.: Clouds and Aerosols, in: Climate Change 2013: The Physical Science Basis, Contribution of Working Group I to the Fifth Assessment Report of the Intergovernmental Panel on Climate Change, edited by: Stocker, T. F., Qin, D., Plattner, G.-K., Tignor, M., Allen, S. K., Boschung, J., Nauels, A., Xia, Y., Bex, V., and Midgley, P. M., Cambridge University Press, Cambridge, United Kingdom and New York, NY, USA, 571–658, doi:10.1017/CBO9781107415324.016, 2013. 8297, 8298, 8312

Bourassa, A. E., Degenstein, D. A., and Llewellyn, E. J.: Climatology of the subvisual cirrus clouds as seen by OSIRIS on Odin, Adv. Sp. Res., 36, 807–812, doi:10.1016/j.asr.2005.05.045, 2005. 8300

Bourassa, A. E., Degenstein, D. A., Elash, B. J., and Llewellyn, E. J.: Evolution of the stratospheric aerosol enhancement following the eruptions of Okmok and Kasatochi: Odin-OSIRIS measurements, J. Geophys. Res. D Atmos., 115, D00L03, doi:10.1029/2009JD013274, 2010. 8326

Bourassa, A. E., Robock, A., Randel, W. J., Deshler, T., Rieger, L. A., Lloyd, N. D., Llewellyn, E. J. T., and Degenstein, D. A.: Large volcanic aerosol load in the stratosphere linked to Asian monsoon transport., Science, 337, 78–81, doi:10.1126/science.1219371, 2012. 8325

Bovensmann, H., Burrows, J. P., Buchwitz, M., Frerick, J., Noël, S., Rozanov, V. V., Chance, K. V., and Goede, A. P. H.: SCIAMACHY: Mission Objectives and Measurement Modes, J. Atmos. Sci., 56, 127–150, doi:10.1175/1520-0469(1999)056<0127:SMOAMM>2.0.CO;2, 1999. 8299, 8302

Bramstedt, K., Noël, S., Bovensmann, H., Gottwald, M., and Burrows, J. P.: Precise pointing knowledge for SCIAMACHY solar occultation measurements, Atmos. Meas. Tech., 5, 2867–2880, doi:10.5194/amt-5-2867-2012, 2012. 8304

Burrows, J. P., Hölzle, E., Goede, A. P. H., Visser, H., and Fricke, W.: SCIAMACHY – scanning imaging absorption spectrometer for atmospheric chartography, Acta Astronaut., 35, 445–451, doi:10.1016/0094-5765(94)00278-T, 1995. 8299, 8302

Chepfer, H., Bony, S., Winker, D., Cesana, G., Dufresne, J. L., Minnis, P., Stubenrauch, C. J., and Zeng, S.: The GCM Oriented CALIPSO Cloud Product (CALIPSO-GOCCP), J. Geophys. Res., 115, D00H16, doi:10.1029/2009JD012251, 2010. 8300, 8317, 8318

AMTD
8, 8295–8352, 2015

Clarisse, L., Coheur, P.-F., Prata, F., Hadji-Lazaro, J., Hurtmans, D., and Clerbaux, C.: A unified approach to infrared aerosol remote sensing and type specification, Atmos. Chem. Phys., 13, 2195–2221, doi:10.5194/acp-13-2195-2013, 2013. 8326

Cziczo, D. J., Froyd, K. D., Hoose, C., Jensen, E. J., Diao, M., Zondlo, M. a, Smith, J. B., Twohy, C. H., and Murphy, D. M.: Clarifying the dominant sources and mechanisms of cirrus cloud formation, Science, 340, 1320–1324, doi:10.1126/science.1234145, 2013. 8298

Davis, S. M., Liang, C. K., and Rosenlof, K. H.: Interannual variability of tropical tropopause layer clouds, Geophys. Res. Lett., 40, 2862–2866, doi:10.1002/grl.50512, 2013. 8299

Doeringer, D., Eldering, A., Boone, C. D., González Abad, G., and Bernath, P. F.: Observation of sulfate aerosols and SO_2 from the Sarychev volcanic eruption using data from the Atmospheric Chemistry Experiment (ACE), J. Geophys. Res., 117, D03203, doi:10.1029/2011JD016556, 2012. 8326

Ebojie, F., von Savigny, C., Ladstätter-Weißenmayer, A., Rozanov, A., Weber, M., Eichmann, K.-U., Bötel, S., Rahpoe, N., Bovensmann, H., and Burrows, J. P.: Tropospheric column amount of ozone retrieved from SCIAMACHY limb-nadir-matching observations, Atmos. Meas. Tech., 7, 2073–2096, doi:10.5194/amt-7-2073-2014, 2014. 8301

European Space Agency: Readme file for SCIAMACHY Level 2 version 5.02 products – Issue 1.2 (ENVI-GSOP-EOGD-QD-13-0118), 2013. 8301, 8310

Fischer, H., Birk, M., Blom, C., Carli, B., Carlotti, M., von Clarmann, T., Delbouille, L., Dudhia, A., Ehhalt, D., Endemann, M., Flaud, J. M., Gessner, R., Kleinert, A., Koopman, R., Langen, J., López-Puertas, M., Mosner, P., Nett, H., Oelhaf, H., Perron, G., Remedios, J., Ridolfi, M., Stiller, G., and Zander, R.: MIPAS: an instrument for atmospheric and climate research, Atmos. Chem. Phys., 8, 2151–2188, doi:10.5194/acp-8-2151-2008, 2008. 8305

Fueglistaler, S., Dessler, A., Dunkerton, T., Folkins, I., Fu, Q., and Mote, P.: Tropical Tropopause Layer, Rev. Geophys., 47, 1–31, doi:10.1029/2008RG000267, 2009. 8298

Generoso, S., Bey, I., Labonne, M., and Breon, F.-M.: Aerosol vertical distribution in dust outflow over the Atlantic: Comparisons between GEOS-Chem and Cloud-Aerosol Lidar and Infrared Pathfinder Satellite Observation (CALIPSO), J. Geophys. Res., 113, D24209, doi:10.1029/2008JD010154, 2008. 8317

Global Volcanism Program: Report on Rabaul (Papua New Guinea), in: Bulletin of the Global Volcanism Network, edited by: Wunderman, R., Smithsonian Institution, Washington, DC, USA, Vol. 31, doi:10.5479/si.GVP.BGVN200609-252140, 2006. 8319

AMTD
8, 8295–8352, 2015

Gottwald, M., Krieg, E., von Savigny, C., Noël, S., Bovensmann, H., and Bramstedt, K.: Determination of SCIAMACHY Line of Sight Misalignments, Proceedings of the Envisat Atmospheric Science Conference, Montreux, Switzerland, 23–27 April 2007, ESA SP-636, 2007. 8304

Gottwald, M. and Bovensmann, H.: SCIAMACHY – Exploring the Changing Earth's Atmosphere, Springer, ISBN 978-90-481-9895-5, 2011. 8302

Haywood, J. M., Jones, A., Clarisse, L., Bourassa, A., Barnes, J., Telford, P., Bellouin, N., Boucher, O., Agnew, P., Clerbaux, C., Coheur, P., Degenstein, D., and Braesicke, P.: Observations of the eruption of the Sarychev volcano and simulations using the HadGEM2 climate model, J. Geophys. Res., 115, D21212, doi:10.1029/2010JD014447, 2010. 8326

Hommel, R., Eichmann, K.-U., Aschmann, J., Bramstedt, K., Weber, M., von Savigny, C., Richter, A., Rozanov, A., Wittrock, F., Khosrawi, F., Bauer, R., and Burrows, J. P.: Chemical ozone loss and ozone mini-hole event during the Arctic winter 2010/2011 as observed by SCIAMACHY and GOME-2, Atmos. Chem. Phys., 14, 3247–3276, doi:10.5194/acp-14-3247-2014, 2014. 8319

IPCC: Climate Change 2013: The Physical Science Basis, Contribution of Working Group I to the Fifth Assessment Report of the Intergovernmental Panel on Climate Change, edited by: Stocker, T. F., Qin, D., Plattner, G.-K., Tignor, M., Allen, S. K., Boschung, J., Nauels, A., Xia, Y., Bex, V., and Midgley, P. M., Cambridge UniversityPress, Cambridge, United Kingdom and New York, NY, USA, 1535 pp., doi:10.1017/CBO9781107415324, 2013. 8297, 8299

Kaiser, J. W., von Savigny, C., Eichmann, K.-U., Noël, S, Bovensmann, H., Frerick, J., and Burrows, J. P.: Satellite-pointing retrieval from atmospheric limb-scattering of solar UV-B radiation, Can. J. Phys., 82, 1041–1052, doi:10.1139/p04-071, 2004b. 8304

Koelemeijer, R. B. A., Stammes, P., Hovenier, J. W., and de Haan, J. F.: Global distributions of effective cloud fraction and cloud top pressure derived from oxygen A band spectra measured by the Global Ozone Monitoring Experiment: Comparison to ISCCP data, J. Geophys. Res., 107, 4151, doi:10.1029/2001JD000840, 2002. 8299

Kokhanovsky, A. A.: Optical properties of terrestrial clouds, Earth-Sci. Rev., 64, 189–241, doi:10.1016/S0012-8252(03)00042-4, 2004. 8309

Kokhanovsky, A. A. and Rozanov, V. V.: The reflection function of optically thick weakly absorbing turbid layers: A simple approximation, J. Quant. Spectrosc. Radiat. Transf., 77, 165–175, doi:10.1016/S0022-4073(02)00085-7, 2003. 8310

AMTD
8, 8295–8352, 2015

Kokhanovsky, A. A., Rozanov, V. V., Burrows, J. P., Eichmann, K. U., Lotz, W., and Vountas, M.: The SCIAMACHY cloud products: Algorithms and examples from ENVISAT, Adv. Space Res., 36, 789–799, doi:10.1016/j.asr.2005.03.026, 2005. 8305, 8307

Kokhanovsky, A. A., Jourdan, O. and Burrows, J. P.: The cloud phase discrimination from a satellite, IEEE Geosci. Remote Sens. Lett., 3, 103–106, doi:10.1109/LGRS.2005.858487, 2006. 8307

Kravitz, B., Robock, A., Bourassa, A., Deshler, T., Wu, D., Mattis, I., Finger, F., Hoffmann, A., Ritter, C., Bitar, L., Duck, T. J., and Barnes, J. E.: Simulation and observations of stratospheric aerosols from the 2009 Sarychev volcanic eruption, J. Geophys. Res., 116, D18211, doi:10.1029/2010JD015501, 2011. 8325

Leahy, L. V., Wood, R., Charlson, R. J., Hostetler, C. A., Rogers, R. R., Vaughan, M. A., and Winker, D. M.: On the nature and extent of optically thin marine low clouds, J. Geophys. Res. Atmos., 117, 1–20, doi:10.1029/2012JD017929, 2012. 8299

Lelli, L., Kokhanovsky, A. A., Rozanov, V. V., Vountas, M., Sayer, A. M., and Burrows, J. P.: Seven years of global retrieval of cloud properties using space-borne data of GOME, Atmos. Meas. Tech., 5, 1551–1570, doi:10.5194/amt-5-1551-2012, 2012. 8299, 8305, 8309

Lelli, L.: Studies of global cloud field using measurements of GOME, SCIAMACHY and GOME-2, PhD thesis, IUP, available at: http://elib.suub.uni-bremen.de/edocs/00103470-1.pdf, 2013. 8309

Lelli, L., Kokhanovsky, A. A., Rozanov, V. V., Vountas, M., and Burrows, J. P.: Linear trends in cloud top height from passive observations in the oxygen A-band, Atmos. Chem. Phys., 14, 5679–5692, doi:10.5194/acp-14-5679-2014, 2014. 8320

Liebing, P., Bramstedt, K., Noël, S., Rozanov, V., Bovensmann, H., and Burrows, J. P.: Polarization data from SCIAMACHY limb backscatter observations compared to vector radiative transfer model simulations, Atmos. Meas. Tech., 6, 1503–1520, doi:10.5194/amt-6-1503-2013, 2013. 8303

Liou, K. N.: Cirrus clouds and climate, Yearbook of Science and Technology, McGraw-Hill, New York, USA, 51–53, 2005. 8311

Massie, S., Gille, J., Khosravi, R., Lee, H., Kinnison, D., Francis, G., Nardi, B., Eden, T., Craig, C., Halvorson, C., Coffey, M., Packman, D., Cavanaugh, C., Craft, J., Dean, V., Ellis, D., Barnett, J., Hepplewhite, C., Lambert, A., Manney, G., Strawa, A., and Legg, M.: High Resolution Dynamics Limb Sounder observations of polar stratospheric clouds and subvisible cirrus, J. Geophys. Res., 112, D24S31, doi:10.1029/2007JD008788, 2007. 8298, 8300

AMTD
8, 8295–8352, 2015

Mateshvili, N., Fussen, D., Mateshvili, G., Mateshvili, I., Vanhellemont, F., Kyrölä, E., Tukiainen, S., Kujanpää, J., Bingen, C., Robert, C., Tétard, C., and Dekemper, E.: Nabro volcano aerosol in the stratosphere over Georgia, South Caucasus from ground-based spectrometry of twilight sky brightness, Atmos. Meas. Tech., 6, 2563–2576, doi:10.5194/amt-6-2563-2013, 2013. 8325

Mattis, I., Siefert, P., Müller, D., Tesche, M., Hiebsch, A., Kanitz, T., Schmidt, J., Finger, F., Wandinger, U., and Ansmann, A.: Volcanic aerosol layers observed with multiwavelength Raman lidar over central Europe in 2008–2009, J. Geophys. Res., 115, D00L04, doi:10.1029/2009JD013472, 2010. 8325

Normand, E. N., Wiensz, J. T., Bourassa, A. E., and Degenstein, D. A.: Cloud discrimination in probability density functions of limb-scattered sunlight measurements, Atmos. Meas. Tech., 6, 3359–3368, doi:10.5194/amt-6-3359-2013, 2013. 8300

Raspollini, P. and Ceccherini, S.: Configuration Management of MIPAS L2 Auxiliary Data Files, Tech. note, TN-IFAC-GS0302, issue 6, 2011. 8306

Reuter, M. and Pfeifer, S.: Moments from space captured by MSG SEVIRI, Int. J. Remote Sens., 32, 4131–4140, doi:10.1080/01431161.2011.566288, 2011. 8316

Rossow, W. B. and Schiffer, R. A.: Advances in understanding clouds from ISCCP, B. Am. Meteorol. Soc., 80, 2261–2287, 1999. 8299, 8311, 8321

Rozanov, A., Weigel, K., Bovensmann, H., Dhomse, S., Eichmann, K.-U., Kivi, R., Rozanov, V., Vömel, H., Weber, M., and Burrows, J. P.: Retrieval of water vapor vertical distributions in the upper troposphere and the lower stratosphere from SCIAMACHY limb measurements, Atmos. Meas. Tech., 4, 933–954, doi:10.5194/amt-4-933-2011, 2011. 8301

Rozanov, V. V. and Kokhanovsky, A. A.: Semianalytical cloud retrieval algorithm as applied to the cloud top altitude and the cloud geometrical thickness determination from top-of-atmosphere reflectance measurements in the oxygen A band, J. Geophys. Res., 109, D05202, doi:10.1029/2003JD004104, 2004. 8299, 8305

Rozanov, V. V., Rozanov, A. V., Kokhanovsky, A. A., and Burrows, J. P.: Radiative transfer through terrestrial atmosphere and ocean: Software package SCIATRAN, J. Quant. Spectrosc. Radiat. Transf., 133, 13–71, doi:10.1016/j.jqsrt.2013.07.004, 2014. 8309, 8310

Sassen, K. and Cho, B. S.: Subvisual-Thin Cirrus Lidar Dataset for Satellite Verification and Climatological Research, J. Appl. Meteor., 31, 1275–1285, 1992. 8298

AMTD
8, 8295–8352, 2015

Sassen, K., Wang, Z., and Liu, D.: Cirrus clouds and deep convection in the tropics: Insights from CALIPSO and CloudSat, J. Geophys. Res., 114, D00H06, doi:10.1029/2009JD011916, 2009. 8298, 8321

Sembhi, H., Remedios, J., Trent, T., Moore, D. P., Spang, R., Massie, S., and Vernier, J.-P.: MIPAS detection of cloud and aerosol particle occurrence in the UTLS with comparison to HIRDLS and CALIOP, Atmos. Meas. Tech., 5, 2537–2553, doi:10.5194/amt-5-2537-2012, 2012. 8300, 8306, 8322

Sonkaew, T., Rozanov, V. V., von Savigny, C., Rozanov, A., Bovensmann, H., and Burrows, J. P.: Cloud sensitivity studies for stratospheric and lower mesospheric ozone profile retrievals from measurements of limb-scattered solar radiation, Atmos. Meas. Tech., 2, 653–678, doi:10.5194/amt-2-653-2009, 2009. 8300, 8310

Spang, R., Riese, M., Eidmann, G., Offermann, D., Pfister, L., and Wang, P. H.: CRISTA observations of cirrus clouds around the tropopause, J. Geophys. Res., 107, 8174, doi:10.1029/2001JD000698, 2002. 8306

Spang, R., Remedios, J. J., Tilmes, S., and Riese, M.: MIPAS observation of polar stratospheric clouds in the Arctic 2002/2003 and Antarctic 2003 winters, Adv. Space Res., 36, 868–878, 2005. 8306

Spang, R., Arndt, K., Dudhia, A., Höpfner, M., Hoffmann, L., Hurley, J., Grainger, R. G., Griessbach, S., Poulsen, C., Remedios, J. J., Riese, M., Sembhi, H., Siddans, R., Waterfall, A., and Zehner, C.: Fast cloud parameter retrievals of MIPAS/Envisat, Atmos. Chem. Phys., 12, 7135–7164, doi:10.5194/acp-12-7135-2012, 2012. 8300, 8306, 8316, 8320, 8323

Stubenrauch, C., Rossow, W., Kinne, S., and the GEWEX cloud assessment group: Assessment of Global Cloud Datasets from Satellites report, WCRP Report No. 23/2012, 2012. 8300, 8305

Stubenrauch, C. J., Rossow, W. B., Kinne, S., Ackerman, S., Cesana, G., Chepfer, H., Di Girolamo, L., Getzewich, B., Guignard, A., Heidinger, A., Maddux, B. C., Menzel, W. P., Minnis, P., Pearl, C., Platnick, S., Poulsen, C., Riedi, J., Sun-Mack, S., Walther, A., Winker, D., Zeng, S., and Zhao, G.: Assessment of Global Cloud Datasets from Satellites: Project and Database Initiated by the GEWEX Radiation Panel, B. Amer. Meteorol. Soc., 94, 1031–1049, doi:10.1175/BAMS-D-12-00117.1, 2013. 8297, 8300

von Savigny, C., Kaiser, J. W., Bovensmann, H., Burrows, J. P., McDermid, I. S., and Leblanc, T.: Spatial and temporal characterization of SCIAMACHY limb pointing errors during the first

AMTD
8, 8295–8352, 2015

three years of the mission, Atmos. Chem. Phys., 5, 2593–2602, doi:10.5194/acp-5-2593-2005, 2005. 8304
von Savigny, C., Ulasi, E. P., Eichmann, K.-U., Bovensmann, H., and Burrows, J. P.: Detection and mapping of polar stratospheric clouds using limb scattering observations, Atmos. Chem. Phys., 5, 3071–3079, doi:10.5194/acp-5-3071-2005, 2005. 8303, 8307, 8317, 8324
von Savigny, C., Eichmann, K.-U., Robert, C. E., Burrows, J. P., and Weber, M.: Sensitivity of equatorial mesopause temperatures to the 27-day solar cycle, Geophys. Res. Lett., 39, L21804, doi:10.1029/2012GL053563, 2012. 8303
Winker, D. M. and Trepte, C. R.: Laminar cirrus observed near the tropical tropopause by LITE, Geophys. Res. Lett., 25, 3351–3354, doi:10.1029/98GL01292, 1998. 8298
Winker, D. M., Vaughan, M. A., Omar, A., Hu, Y., Powell, K. A., Liu, Z., Hunt, W. H., and Young, S. A.: Overview of the CALIPSO mission and CALIOP data processing algorithms, J. Atmos. Ocean. Technol., 26, 2310–2323, doi:10.1175/2009JTECHA1281.1, 2009. 8300

AMTD
8, 8295–8352, 2015

Table 1. Pairs of corresponding latitude, sun zenith angle (SZA), and relative sun azimuth angle (SAA) of the tangent point in limb measurement geometry for a typical SCIAMACHY orbit (PN: Polar North, MN: Mid-latitude North, ETN: Extra Tropics North, TRO: Tropics, MS: Mid-latitude South, PS: Polar South).

Area	Latitude [°]	SZA [°]	SAA [°]
PN	70	84	22
MN	51	67	39
ETN	36	55	45
TRO	−8	26	83
ETS	−37	41	136
MS	−51	51	148
PS	−80	85	151

AMTD
8, 8295–8352, 2015

Figure 1. The Earth's limb as seen from the International Space Station on 16 June 2010. The ISS Nadir point was in the Aegean Sea at 36.8° N latitude and 27.1° E longitude. Image courtesy of the Image Science & Analysis Laboratory, NASA Johnson Space Center, Mission-Roll-Frame ISS024-E-6137 (http://eol.jsc.nasa.gov).

AMTD
8, 8295–8352, 2015

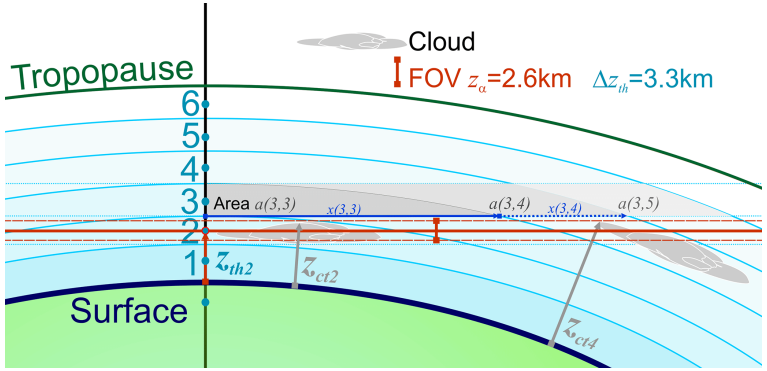

Figure 2. Geometry of a limb measurement. The shells are numbered from the surface to the tropopause (1–6). The field-of-view (FOV), the tangent height step width z_{th}, and cloud top height z_{ct} are overplotted. Examples of shell path lengths x as blue lines and areas a (grey shaded) are also shown. The limb path is a combination of the paths through each shell, here e.g. starting in shell 3, we have the sub-paths $x(3,3)$, $x(3,4)$, and $x(3,5)$ (blue line) depicted.

AMTD
8, 8295–8352, 2015

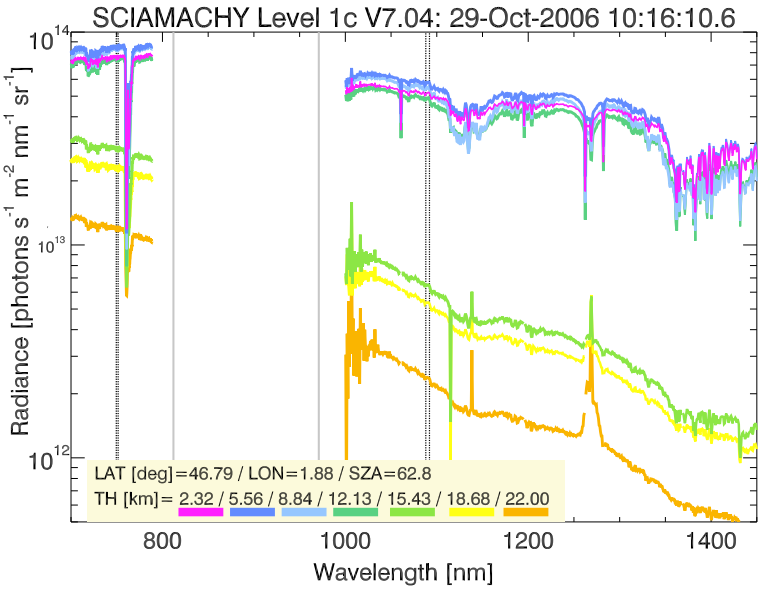

Figure 3. SCIAMACHY limb radiances from channels 4 (700–789 nm) and 6 (1000–1300 nm) at tangent heights (TH) from 2.3 (violet) to 22.0 km (orange). One measurement sequence from 29 October 2006 of the orbit 24 382 (measurement start time 10:16:10.62 UTC) at 46.8° latitude (LAT), 1.9° longitude (LON), and 62.8° sun zenith angle (SZA) from operational Level 1c data version 7.04 (calibration parameters 0–5) has been used. The wavelength bands around 750 and 1090 nm that are used for the cloud retrieval are shown as vertical dashed black lines. The vertical grey lines depict the channel borders.

AMTD
8, 8295–8352, 2015

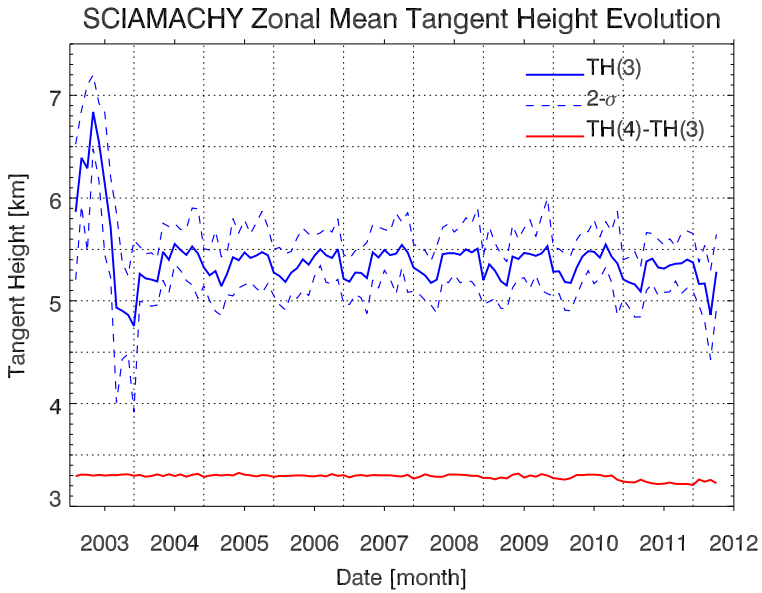

Figure 4. Time series covering the SCIAMACHY mission lifetime of one limb tangent height [km]. TH(3) is e.g. the tangent height with index number 3. Daily means are plotted, taken from one day per month (usually the first day) and made from the first state of 10 orbits of that day. The dashed blue lines depict the corresponding 2-σ standard deviation. The red line shows the difference between 2 adjacent tangent heights.

AMTD
8, 8295–8352, 2015

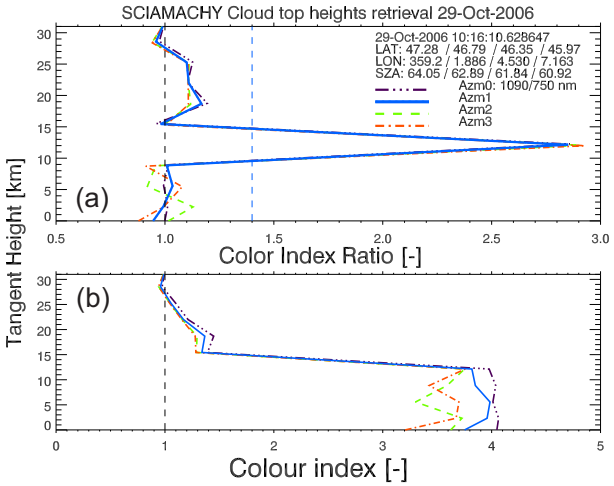

Figure 5. Colour index ratio **(a)** and colour index **(b)** of one SCIAMACHY limb measurement at 29 October 2006 (see Figure above). All four limb profiles that are simultaneously measured in one limb measurement state (AZM 0–3) are shown here.

AMTD
8, 8295–8352, 2015


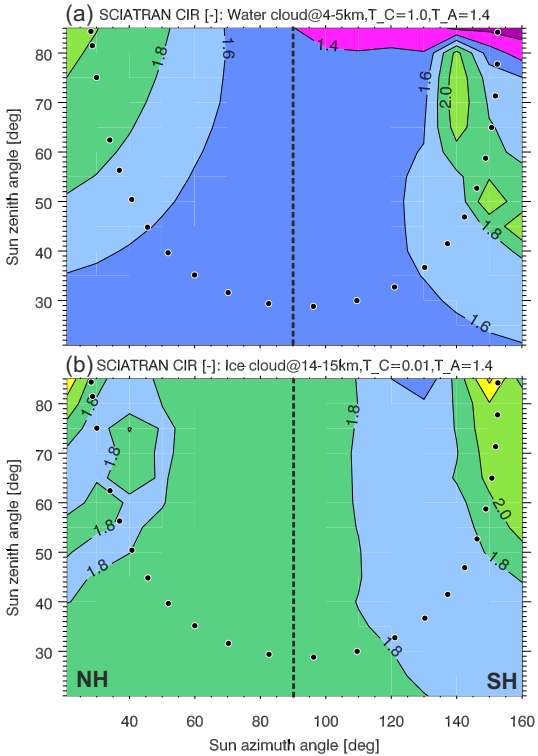

Figure 6. Simulated maximum colour index ratios as a function of sun zenith angle and sun azimuth angle. The radiances were calculated using the SCIATRAN forward model. **(a)** A water cloud with an optical thickness τ_C of 1 between 4 and 5 km altitude is simulated. **(b)** A sub-visual ice cloud with an optical thickness of 0.01 between 14 and 15 km altitude is simulated. The aerosol optical thickness τ_A is taken to be 1.4 at 790 nm. The black and white dots show SCIAMACHY pairs of zenith and azimuth angles along an example orbit. Low azimuth angles are typical for the Northern hemisphere and large angles in the Southern hemisphere.

AMTD
8, 8295–8352, 2015

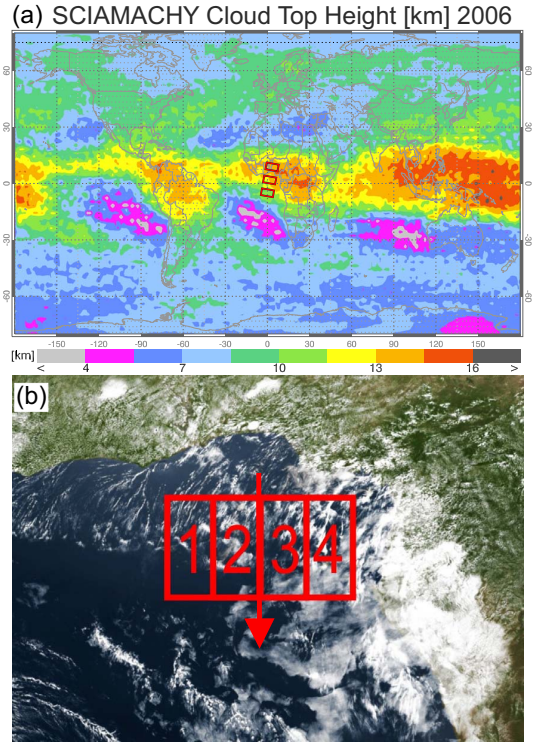

Figure 7. Global distribution of **(a)** gridded annual averaged cloud top heights [km] of 2006 using 2° latitude by 2° longitude grid boxes. The overplotted red rectangles gives an estimate of the size of three consecutive SCIAMACHY limb scans. A picture from SEVIRI on board MSG (Meteosat Second Generation, EUMETSAT) shows part of the African continent **(b)** to illustrate the limb coverage of a cloud field. The overplotted red rectangles give the sizes of the 4 limb measurements of one SCIAMACHY limb scan at the tangent point. The arrow indicates the viewing direction. The MSG picture was contributed by M. Reuter (IUP Bremen) and has been adapted.

AMTD
8, 8295–8352, 2015

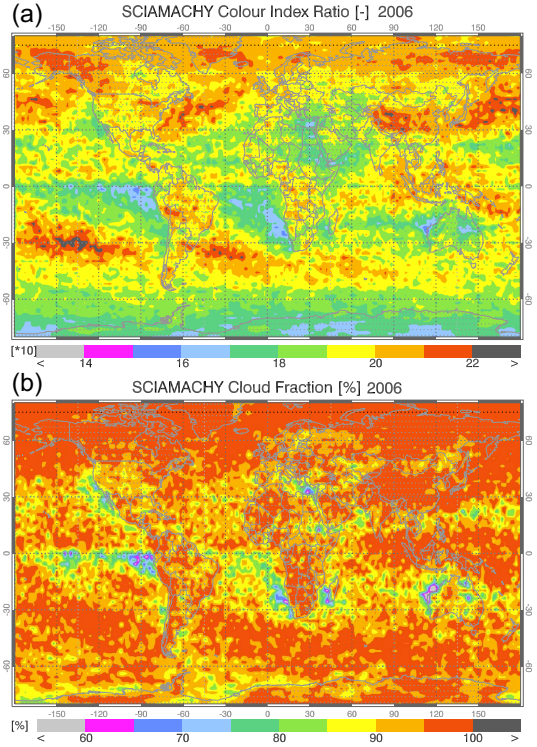

Figure 8. Global annual mean **(a)** the global colour index ratio at cloud top for the year 2006 and gridding parameters as used in Fig. 7 and **(b)** the limb cloud fraction [%].

AMTD
8, 8295–8352, 2015

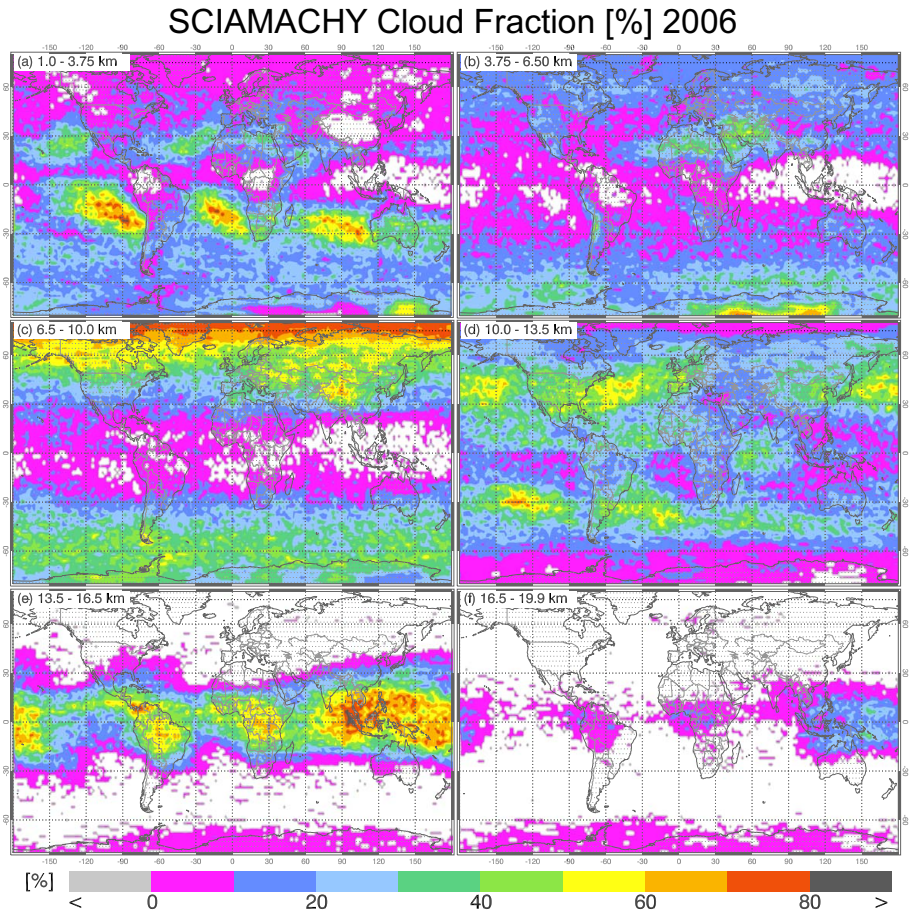

Figure 9. Global annual mean of the SCIAMACHY cloud fraction [%] 2006 for tangent heights between: **(a)** 1.0–3.75 km, **(b)** 3.75–6.5 km, **(c)** 6.5–10.0 km, **(d)** 10–13.5 km, **(e)** 13.5–16.5 km, and **(f)** 16.5–19.9 km.

AMTD
8, 8295–8352, 2015

Cloud top height retrieval using SCIAMACHY limb spectra

K.-U. Eichmann et al.

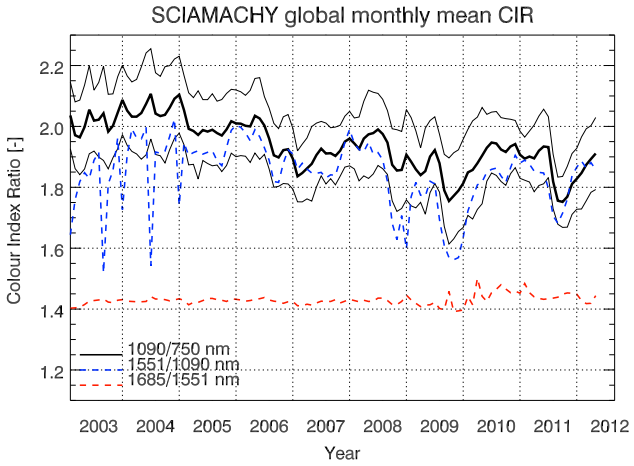

Figure 10. Global monthly averages of the SCIAMACHY colour index ratio CIR for the 1090/750 nm wavelength pair and its 1σ standard deviation. Also plotted are two different CIRs using the ratios of 1551/1090 nm (blue dashed line) and 1685/1551 nm (red dashed line).

AMTD
8, 8295–8352, 2015

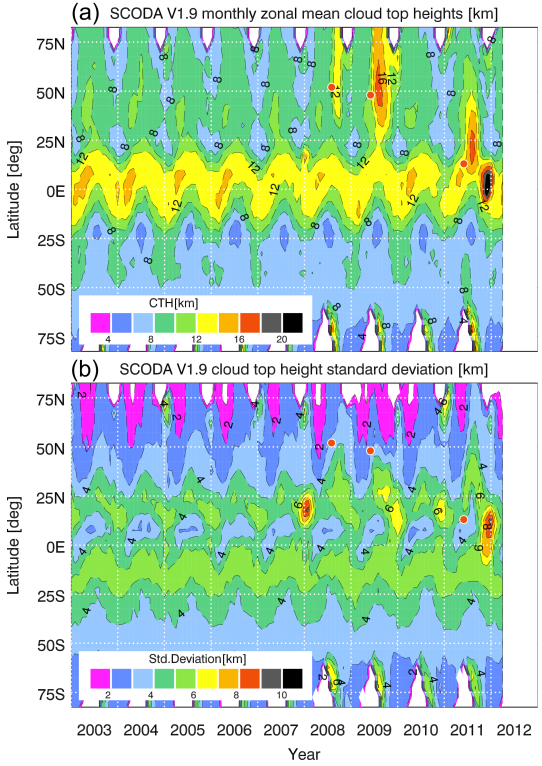

Figure 11. SCIAMACHY/SCODA cloud top height **(a)** and **(b)** 1σ standard deviation [km] for the time period January 2003 to April 2012. Zonal monthly means between 80° S and 80° N were calculated. The red dots depict the start date and latitude of 3 major volcanic eruptions from Kasatochi, Sarychev Peak, and Nabro.

AMTD
8, 8295–8352, 2015

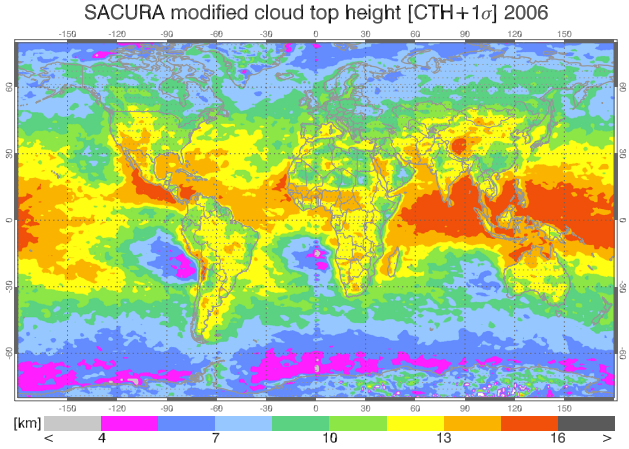

Figure 12. Modified annual mean of the SCIAMACHY/SACURA nadir cloud top height [km] above sea mean level for the period January 2006 to December 2006. The 1σ standard deviation has been added for each grid cell.

AMTD
8, 8295–8352, 2015

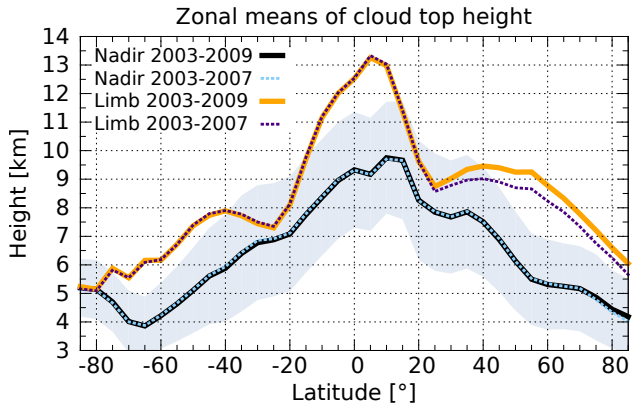

Figure 13. SCODA CTH zonal means averaged over 5 (2003–2007, purple dotted line) and 7 (2003–2009, orange line) years. Also shown are the corresponding SACURA nadir zonal means and the 1-σ intervals. The gap in the northern hemisphere between orange-solid and purple-dotted curves shows the influence of volcanic eruptions in 2008 and 2009.

AMTD
8, 8295–8352, 2015

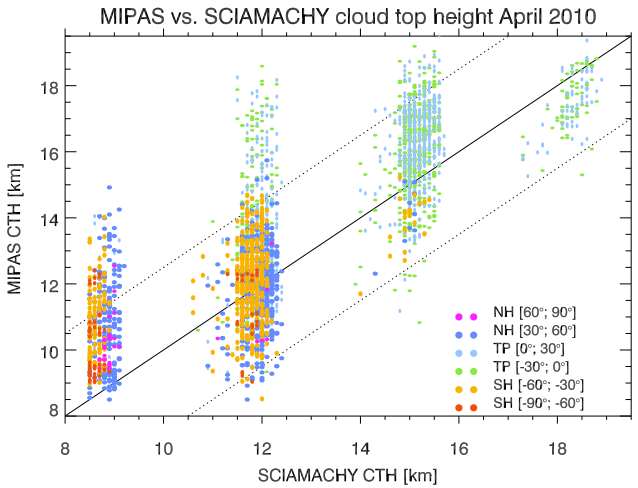

Figure 14. Comparison of co-located cloud top heights from SCIAMACHY and MIPAS measurements for April 2010. The scatter plot shows color-coded measurement pairs divided into six latitude bands (North/South polar, midlatitude and tropical bands, each 30° wide).

AMTD
8, 8295–8352, 2015

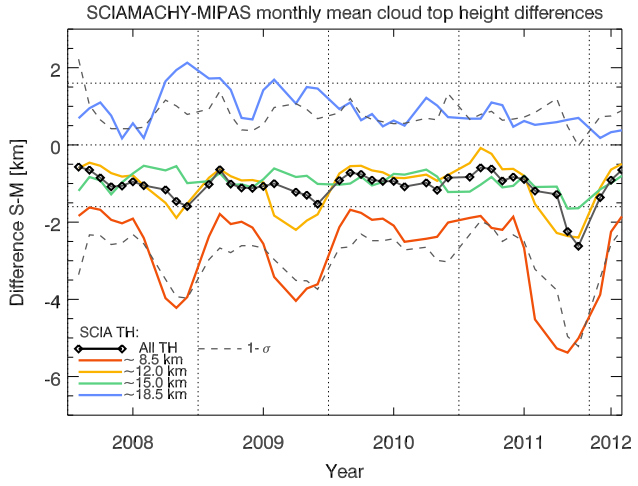

Figure 15. Zonal monthly means of co-located cloud top height differences [%] between MIPAS and SCIAMACHY (grey line, black diamonds) and the corresponding 1σ standard deviation (dashed grey) for the time period between 2008 until the end of mission in 2012. Overplotted are the differences for all SCIAMACHY tangent heights (TH) between 8 and 20 km.

AMTD
8, 8295–8352, 2015

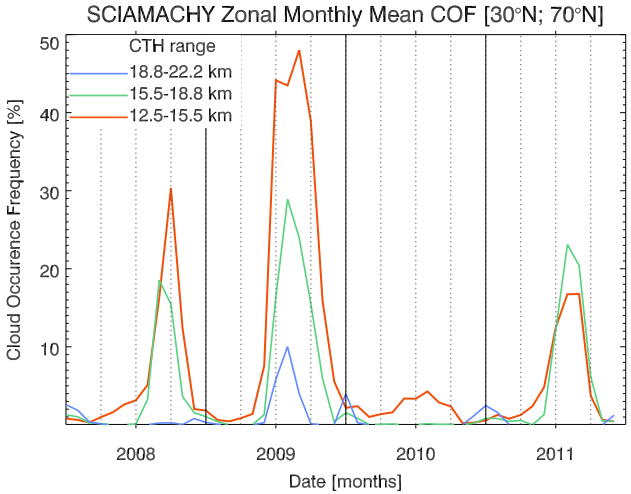

Figure 16. SCIAMACHY occurrence frequencies [%] of the cloud/aerosol scattering layer for 3 different height regimes (12.5–15.5/15.5–18.8/18.8–22.2 km) for the years 2008–2011. Zonal monthly means for the latitude band 30–70° N were calculated.

AMTD
8, 8295–8352, 2015